DEAR MARSHALL

(NASA-CR-174245) ANALYSIS OF PHYSICAL-CHEMICAL PROCESSES GOVERNING SSME INTERNAL FLUID FLOWS Progress Report (CHAM of North America, Inc.) 87 p HC A05/MF A01 CSCL 21H G3/20

N85-14862

Unclas 13032

CHAM OF NORTH AMERICA, INCORPORATED
1525 A Sparkman Drive
Huntsville, Alabama 35805
Telephone 205 830-2620

ANALYSIS OF PHYSICAL-CHEMICAL PROCESSES GOVERNING SSME INTERNAL FLUID FLOWS:

PROGRESS REPORT FOR NOVEMBER 1984

by

A.K. Singhal, S.F. Owens, T. Mukerjee, L.W. Keeton,
C. Prakash, and A.J. Przekwas

December 1984 4045/10

Prepared for:
National Aeronautics and Space Administration
George C. Marshall Space Flight Center
Alabama 35812

NASA COR: Dr. N.C. Costes (ED42)
Contract Number: NAS8-35970

PREFACE

This progress report summarized the work performed during the report period, and discusses the work to be performed during the next report period. It also indicates current problems (if any), and an estimated percentage completion of the work scheduled for the first two years of the contract.

INTRODUCTION

In order to aid the development of current and future (advanced) SSME type engines, it is necessary to improve the understanding of basic issues related with physical-chemical processes of SSME internal flows. Towards this goal, the specific objectives of the subject are:

1. to supply the general-purpose CFD code PHOENICS and the associated interactive graphics package - GRAFFIC.
2. to demonstrate code usage on SSME-related problems to NASA MSFC personnel;
3. to perform computations and analyses of problems relevant to current and future SSME's; and
4. to participate in the development of new physical models of various processes present in SSME components

The total project duration is three years. This is the progress report for the month of November 1984 (i.e. seventh month of the first year of performance).

During November 1984, contractual amendments were received for additional work scope of tasks 2 and 3 and the work was authorized upto April 1986, i.e. upto the end of the second year of the contract.

WORK PERFORMED DURING NOVEMBER, 1984

During the month of November 1984, attention was focussed on Tasks 2, 3, 4 and 5. Accomplishments under each of these tasks are described below.

TASK 2: Interface Codes with MSFC Facility and Personnel

Under this task, the Body Fitted Coordinate (BFC) system of PHOENICS was transferred to MSFC facilities. A one-day training course was held on November 5, 1984. Relevant documentations for this course were handed over to NASA personnel.

TASK 3: Flow Physics Applications

The application of Body Fitted Coordinate (BFC) system of PHOENICS was extended to the SSME Hot Gas Manifold problem with the k-ε model of turbulence.

Results of this calculation, along with those of the constant eddy viscosity calculations, were presented at the following two meetings at NASA MSFC.

1. A meeting arranged by Dr. N.C. Costes for extensive review of CHAM's results by NASA MSFC personnel. The meeting was attended by about 45 persons from ED01, ED11, ED13, ED33, ED41, ED42 and EP23 divisions.

2. The second SSME CFD workshop group meeting held at NASA MSFC on November 28 - 30, 1984. This presentation was attended by about 80 persons from NASA MSFC, LeRC, ARC, Rocketdyne and other contractors.

The required number of copies of the presented material were provided to the organizers of the meetings.

The second major activity under Task 3, was to adapt PHOENICS for SSME Aft Plateform Seal Cavity problem. Details of this problem, with selected results obtained so far with PHOENICS, are presented in Appendix 1. This work was carried out at CHAM with active participation of Mr. Sam Lowry of EP23 division of NASA MSFC, and it was also presented at the SSME CFD meeting on November 28 - 30, 1984.

TASK 4: Thermofluid Analysis of the SSME Preburner

The first phase of the SSME preburner flow analysis based on the two-fluid modeling approach, outlined in the previous progress report, was completed during November, 1984. These results were also presented in the SSME CFD meeting held at NASA MSFC on November 28 - 30, 1984.

To further understand the mixing and combustion processes in the preburner, a single oxygen-hydrogen jet element has been numerically analysed. Single phase multicomponent theory is employed with instantaneous reaction assumed for combustion. Is is found that the oxygen jet can penetrate a distance of upto 40 jet diameters into the preburner. This distance is about 50% of the burner height. Results of this study along with recommendations for further work are presented in Appendix 2.

TASK 5: SSME Global Flow Model

As a first step towards the development of SSME Global Model, a 3-D analysis of the Main Injector Assembly (or LOX Post) region has been done. The complex geometry has been carefully studied and modeled by describing the restrictions in flow area due to the LOX posts in terms of porosities and loss coefficients. A PHOENICS "satellite" and "ground station" set has been developed for this purpose, and the results of this study, along with recommendations for further work, are presented in Appendix 3.

WORK PLANNED FOR DECEMBER 1984

During the next month work will continue on Tasks 2, 3, 4 and 5. For Task 2, necessary assistance to MSFC personnel in using the BFC system will be provided. For Task 3, seal cavity problem will be pursued.

For Task 4, Multi-phase analysis of preburner with emphasis on development of semi-empirical expressions for exchange coefficients, C_M and C_F, will be continued.

For Task 5, the LOX-post region model development will be continued.

CURRENT PROBLEMS

No problems are envisaged which may impede performance of this project.

PROGRESS SUMMARY

A task wise progress status is shown in Table below. Estimated total percentage completion through November is 40% of the first two year's scope of work.

No.	TASK DESCRIPTION	% COMPLETION OF FIRST TWO YEARS EFFORT, AS ON NOVEMBER 30, 1984
1.	Provide PHOENICS & GRAFFIC codes	50
2.	Interface codes with MSFC Facility and Personnel	48
3.	Flow Physics Applications	45
4.	Multi-Fluid (Phase) Model	30
5.	SSME Global Flow Model	15
6.	Reports	Monthly Progress Reports

CHAM

APPENDIX 1

Interim Report

on

Aft-Platform Seal Cavity Flow Analysis

by

L.W. Keeton, S.A. Lowry and J. Ingram

December 11, 1984

SUMMARY

This interim report summarizes the work performed to date on the adaptation of CHAM's computational fluid dynamics code, PHOENICS, to the analysis of flow within the HPFTP aft-platform seal cavity of the SSME.

In particular, the special purpose PHOENICS satellite and ground station specifically formulated for this application are listed and described, and the preliminary results of the first part two-dimensional analyses are presented and discussed.

Planned three-dimensional analyses are also briefly outlined.

1. INTRODUCTION

A computer analysis of the flow within the SSME High Pressure Fuel TurboPump (HPFTP) aft-platform seal cavity is being performed jointly by CHAM and the Turbomachinery Branch of the Structures and Propulsion Laboratory, MSFC. The work has been split into two parts, viz: (a) a 2-dimensional analysis; and (b) an extension to 3-dimensional analysis. This report summarizes briefly the coding of the special purpose PHOENICS code satellite and ground stations specifically formulated for this application. It also describes the preliminary results of the 2-dimensional analyses performed to date, along with a brief outline of the currently proposed 3-dimensional studies.

Thus, this report presents:

1. problem description;
2. numerical model set-up;
3. presentation of results;
4. observations and discussion;
5. comments; and
6. next steps.

2. PROBLEM DESCRIPTION

The main purpose of this study is to predict the temperatures, pressures, and velocities in the SSME HPFTP aft-platform seal cavity for a variety of boundary conditions and geometries. An understanding of this flow field is critical since there are at least two problems in the High Pressure Fuel Pump which are potentially linked to the environment in this region. This cavity is located downstream of the fuel pump's second turbine disk, between the disk and the aft-platform seal, Figure 1. It is an annular region with irregular boundaries as shown in Figure 2. In this cavity, the cold ($150^{o}R$) hydrogen enters due to leakage through the labyrinth seal, and hot ($1300^{o}R$) combustion products (H_2 and H_2O) enter from the gap between consecutive blade shanks. The problems believed to be associated with the flows and temperatures in this region are: 1) cracking of the second stage turbine blade shanks; and 2) hot gas leakage into the stack behind the aft-platform seal.

The questions being addressed by the current analysis relate directly to the pump hardware. Some of the principal questions are listed below:

1. Using the current design how severe is the temperature gradient in the region where the turbine blades are cracking?
2. What effect would a given design modification have on the above gradient?
3. What would be the temperature of any fluid which leaked past the bolts that secure the aft-platform seal to the stack.
4. What is the influence of the known circumferential variation in turbine discharge pressure on the flow pattern (mixing and temperatures) in this region?

Boundary Conditions

In general the aft-platform seal cavity is an axisymmetric annular cavity defined by stationary walls on one side and a rotating disk on the other. Flow comes into the cavity through two inlets, one at the inner radius of the cavity and one near the outer radius of the disk. The flow leaves the region through one or more exits, the principal of which is located around the outer diameter of the cavity (Figure 2). At high rpm (up to 37,000) the flow is a turbulent mixture of hydrogen and water at temperatures ranging from approximately $140^{o}R$ to possibly as high as the turbine exhaust temperature at $1700^{o}R$. Flowrates are on the order of one lbm/sec and pressures are in the range of 4000 psi. The inlet and exit boundary conditions are described qualitatively below. The specific numbers used in this study have been taken directly from the results of the (one-dimensional) system flow analyses described in NASA Report: LMSC - HREC TR D697954, May 1980. The principal data as used in the five two-dimensional PHOENICS test cases performed to date are summarised in Table 1, overleaf.

Table 1

Boundary Conditions for the Five 2-D Test Cases

Parameter	1 Base Case (Average T.D.P.)	2 Average T.D.P. + 150 psi	3 Average T.D.P. - 150 psi	4 Large Hole in A.P.S.	5 Small Hole in A.P.S.
Pressure (psi)					
Exit 1 (o.d.)	3558	3713	3404	3558	3558
Exit 2 (bolts)	-	-	-	3558	3558
Enthalpy (Btu)					
Hot gas inlet	3052	3045	3058	3052	3052
Coolant inlet	314	314	314	314	314
Flow rate (lbm/s)					
Hot gas inlet	3.65	3.29	3.96	3.65	3.65
Coolant inlet	0.359	0.376	0.342	0.359	0.359
Areas (360^0 sq. in)					
Exit 1 (o.d.)	0.307	0.307	0.307	0.307	0.307
Exit 2 (bolts)	-	-	-	.307	.0102
Disc Speed (rpm)	37000	37000	37000	37000	37000

Nomenclature: T.D.P. = Turbine Discharge Pressure; A.P.S. = Aft-Platform Seal

A. Inlets

1) COOLANT INLET: At the inner radius of the cavity, liquid hydrogen flows into the aft-platform seal cavity through a 360 degree labyrinth seal. The source of this hydrogen is the discharge of the High Pressure Fuel Pump. The amount of hydrogen flow is not fixed but will vary with changing cavity pressure and circumferential pressure variations.

2) HOT GAS INLET AT THE BLADE SHANKS: One wall of the cavity is formed by the rotating disk upon which are mounted the second stage turbine blades. At the periphery of this disk a mixture of coolant hydrogen and combustion products enters the cavity through the gap between the shank of one turbine blade and the next. Since there are 58 blades in the second stage disk there are accordingly 58 holes available for this hot gas mixture to flow into the aft-platform seal cavity from the high pressure side of the turbine disk. The flow pattern through these holes is complex since the shanks of the blades are curved and the disk itself is rotating at up to 37,000 rpm. In addition, the composition of this fluid mixture is difficult to determine since it arrives via a network of flow paths which originate from both the fuel pump discharge and the fuel pump turbine gasses.

B. Outlets

1) EXIT GAP BETWEEN THE OUTER DIAMETER OF THE AFT-PLATFORM SEAL AND THE BLADES: The flow which exits through the 360 degree gap between the outer diameter of the aft-platform seal and the turbine blades depends on the size and shape of the gap and the pressure drop from the cavity to the turbine exhaust. When this gap is the only exit, the total outflow through the gap must, of course, equal the sum of what enters the cavity through the labyrinth seal and the blade shanks. In any case, the actual flow through this gap at a given location will respond to changes in the overall turbine discharge pressure, the circumferential variation in turbine discharge pressure, and any changes in the width of the gap. The latter could be due to a number of different causes, including: sideloads, dynamics, machining tolerances, eccentricity, or thermal expansion.

2) SECONDARY EXIT HOLE: In some cases the aft-platform seal is modeled with a second exit to simulate either a leak or else a design modification. So far all the cases which have been run place the secondary exit next to the

bolts which secure the aft-platform to the lift-off seal stack (Figure 2). The flow through this hole also depends on its size and shape and on the downstream pressure which, thus far, has been assumed to equal the turbine exhaust pressure.

3. NUMERICAL MODEL SET UP

CHAM's general-purpose computational fluid dynamics code, PHOENICS, has been employed for all the numerical studies described herein. To use PHOENICS, special purpose 'satellite' and 'ground station' sub-programs must be formulated whereby the built-in features can either be turned on or off or modified, as necessary. The special purpose satellite and ground stations formulated specifically for the HPFTP aft-platform seal cavity two-dimensional study are listed, in full, in a separate report: CHAM 4045/9. These two subprograms are extensively annotated (via built-in 'COMMENT' statements) such as to make them self-explanatory when read in conjunction with the PHOENICS User's Manual. Consequently, no detailed line-by-line description is given here; however, the most relevant features are described below.

The first part (2-D) calculations described herein have been performed by using the 2-dimensional y/z, polar coordinate option of the code. Figure 3 shows the selected 2-dimensional grid distribution. There are 1120 control cells, with 40 and 28 cells in the radial (IY) and axial (IZ) directions, respectively. Due to the (initially) assumed cyclic symmetry of the problem, only one control cell is required in the circumferential (IX) direction. However, to enable correct account to be taken of the wall shear stresses acting on the fluid entering between the blade shanks, the circumferential extent of the calculation domain is taken to be equal to the space between 2 consecutive blades (i.e. an angle of $1/58 \times 2\times\pi$ degrees, where 58 = total number of blades).

As depicted in Figure 2, the 'cold' liquid hydrogen coolant enters axially, through the labrinth seal, at the bottom of the cavity. This then mixes with the supply of 'hot' hydrogen and water vapor mixture that enters the cavity from between the blade shanks located at the outermost extremity of the rotating disc. The mixture of these two streams of fluid then exits beneath the blade tips, as shown in Figure 2.

Assumptions/Model Details

The major assumptions and salient features of the physical models and the boundary conditions employed are described below.

1. All boundary surfaces (both stationary and rotating) have been assumed to be adiabatic.

2. The hydrogen and water vapor are treated as a single homogeneous fluid with mixture properties (density and laminar viscosity) and temperature deduced from the calculated mixture enthalpy and specified hydrogen and water property curve fit data as described in Appendix A.

3. The turbulence effects are presented by way of the two-equation (k-ε) model of turbulence. In this model, two parameters, viz: the turbulence kinetic energy, k, and its dissipation rate, ε, are computed from differential transport equations. Thus, it has the capability of representing both the local and history effects. The effective viscosity is expressed as:

$$\mu_{eff} = \mu + C_{\mu} \rho \ k^2/\varepsilon$$

where C_{μ} is an empirical constant and ρ is the local mixture density. In addition, four other empirical constants are assigned the values as recommended in original publications.

4. All boundary surfaces of irregular shape are accommodated in the present calculations by use of "cell porosities". In this approach, each control cell is characterised by a set of fractions, in the range from 0 to 1. These fractions determine the proportion of the cell volume which is available for occupancy by the fluid, and the proportion of each cell-face area available for flow from the cell to its neighbor in a given direction. This practice is much more rigorous and accurate than the practice of using rectangular steps.

5. The wall shear stress is calculated by using the conventional wall functions which are based on the assumptions of the logarithmic law of the wall. For partially blocked control cells, the wall stress is calculated for the projected surfaces parallel to velocity components.

   It should be noted that the PHOENICS built-in process for determining wall shear stress is restricted to a finite number of special regions, to be set via the satellite subroutine. For the complex aft-platform seal geometry many such special regions would be necessary, in excess of the built-in maximum, and a special PHOENICS user sub-program was written for the current problem to overcome this restriction. This user sub-program (GWALL) performs the identical job as the built-in PHOENICS 'WALL' subroutine but is used via the PHOENICS GROUND station. A listing of GWALL is also included in CHAM Report 4045/9.

6. In PHOENICS, an iterative finite-difference solution procedure is employed to solve the governing differential equations together with the above mentioned relations. The method is based on a fully implicit, conservative formulation. As a result there is no restriction on the selection of grid and magnitude of time steps.

   The variables calculated and/or solved-for (and printed) in the seal cavity flow calculation included the following:

   a. the fluid velocities in the 3-coordinate directions;

   b. the mixture enthalpy and deduced temperature;

   c. the (mass) concentration of water vapor;

   d. the turbulent kinetic energy and its dissipation rate;

   e. the static and total pressures;

   f. the mixture density and separate densities of both the hydrogen and water vapor; and

   g. the effective viscosity.

7. Boundary conditions are:

   a. prescribed mass flowrate, velocities, enthalpy, mixture ratio and turbulence parameters at all inlets;

   b. prescribed exit pressure at all outlets; and

   c. the incoming fluid enclosed between the blade shanks is assumed to rotate at the same speed as the disc.

8. The (phase-change) freezing of the water is not accounted for; any water at temperatures below freezing is given the properties (density etc.) of liquid water at freezing.

4. PRESENTATION OF RESUTLS

Selected base case (Test case 2 - with average turbine discharge pressure boundary conditions from NASA Report: LMSC - HREC TR 697954, May, 1980) results are shown in Figures 4 to 8. Figure 4 depicts the velocity vectors and streamlines throughout the cavity and Figure 5 shows a magnified picture of the region around the blade shanks and principal exit. Figures 6 to 8 depict the contours of constant temperature, mass concentration of H_2O, and static pressure, respectively. The results for the next two test cases (2 and 3) with boundary conditions pertinent to a ± 150 psi change in turbine discharge pressure are qualitatively indistinguishable from the base case calculations and are not therefore presented.

Test case 4 involves the introduction of a postulated 2nd exit located beneath the bolt shanks that secure the aft-platform seal to the stack (see Figure 2). This hole is taken to be of the same size as the principal exit adjacent to the blades. Selected results for this case are presented in Figures 9 to 11. Figure 9 depicts the velocity vector and streamlines within the cavity with a magnifed view of the blade shank region shown in Figure 10. Figure 11 depicts the contours of constant temperature.

Test case 5 is the same as test case 4 (i.e. with a 2nd exit hold) but with a supposed much smaller 2nd exit hole size to simulate "leakage" around the bolts. The results for this case are depicted in Figures 12 to 14. Again, Figure 12 shows velocity vectors and streamlines with an expanded view of the shank region in Figure 13, and Figure 14 whows the constant temperature lines.

5. OBSERVATIONS AND DISCUSSION

The results of the two-dimensional (unmodified) base case (Figure 4) show that the bulk of the cavity is taken up with a large recirculating zone with several smaller vortices scattered throughout. The "hot" combustion products enter through the blade shank and exit back to the exhaust manifold without entering the cavity below. This is also apparrent in Figure 5 where the two streams of "hot" and "cold" fluid are seen to intersect and shear in the region between the blade shanks and seal o.d. The expected severe temperature gradient in this region is clearly shown in Figure 6, where a temperature rise of 300 to 1275^{o}R across the shanks is seen taking place across the shear layer where the two fluid streams meet. This is the region where blade cracking has has been found and the present base case model results support the idea that this could be due to the severe thermal stresses that would result from such a sharp temperature gradient. Figure 7 depicts the contours of mass concentration of water vapour showing that only a negligable amount (less than 0.1% by mass) reaches the cavity region from the hot gas inlet where approximately 44% (by mass) of the incoming homogenous mixture is water. The isobars of static pressure are shown in Figure 8 indicating a rise (due to the centrifuge effect of the rotating disc) from cold inlet to hot inlet across the disc of approximately 30 psi. The pressure drop across the exit is approximately 650 psi, which agrees well with expectations in NASA Report LMSC - HREC TR D 697954, May 1980.

The consequences of introducing a 2nd exit hold in the cavity are quite dramatic as shown in Figures 9 to 11. The hot gases from between the blade shanks make almost a 50:50 split with half exiting from each of the 2 exits. This shows that the centrifugal (or "pumping") effect of the rotating disc is not large enough to inhibit the radially inward flow to the second exit hole. The beneficial influence this flow "splitting" has on the severe temperature gradient at the blade shanks is apparent in Figure 11 indicating that a 2nd exit would probably reduce the undesirable temperature gradient in this area quite effectively. This effect, however, is proportional to the 2nd hole size as shown in Figures 12 to 14 where the 2nd hole size is approximately 1/30th of that in Figures 9 to 11. The flow in the cavity in this case is very similar to the flow with no hole present (Figures 4 through 6) with the reduction in the temperature gradient not much reduced at the blade shanks.

6. COMMENTS

The two-dimensional results show that for the unmodified seal configuration there is a severe temperature gradient at the blade shanks. In the interior of the cavity there is a large recirculation flow which creates an isothermal region that is slightly warmer than the cold inlet temperature. Within this recirculation zone there is evidence of water which has diffused from the hot gas inlet.

If a hole is introduced in the cavity (see Figure 2) then the recirculation zone is surpressed as hot fluid from the blade shanks flows radially inward and exits through this secondary exit. The relative amount of fluid which is diverted to this second exit is roughly proportional to its area relative to the area of the first exit. The implication is that the pumping action of the disk is not strong enough to significantly inhibit radially inward flow. Given a large enough second exit the flow pattern and temperature gradient can be changed dramatically as demonstrated by the results in Figures 4 to 14.

7. NEXT STEPS

At the time of writing of this interim report, the extension of the PHOENICS satellite and ground station subroutines to simulate the aft-platform seal three-dimensionally have been completed and some initial calculations with assymmetric boundary conditions have been performed. These results

are being studied and, for time economy reasons, are not presented here.

In the next month it is proposed that NASA MSFC and CHAM meet to determine exactly what geometry and boundary conditions are to be studied with the 3-D model. These results will be documented and presented separately.

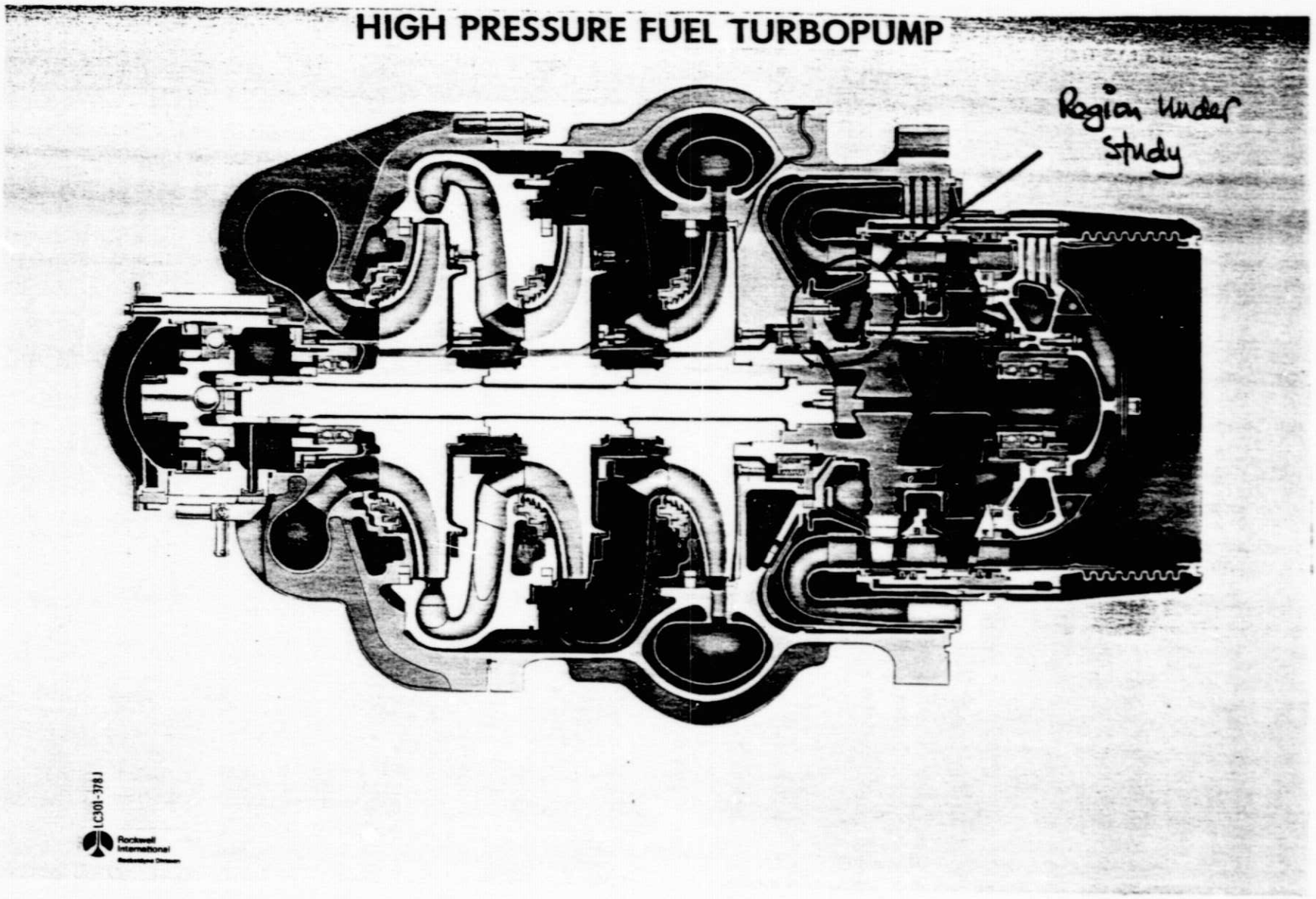

Figure 1 The HPFTP showing Aft-Platform Seal Cavity

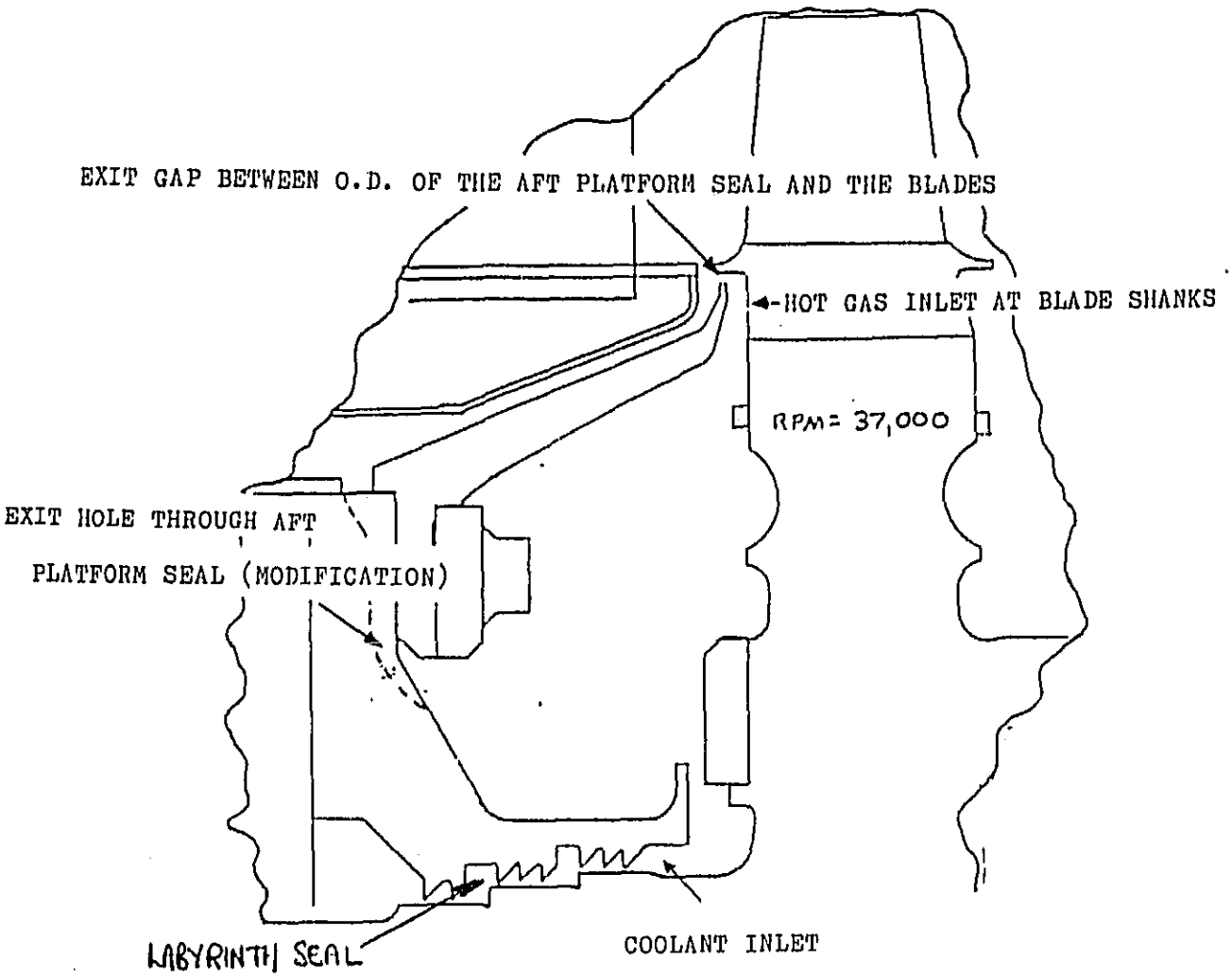

Figure 2 Aft. Platform Seal Geometry.

ORGANIZATION	MARSHALL SPACE FLIGHT CENTER	NAME
CHAM/NASA	SSME HIGH PRESSURE FUEL PUMP AFT PLATFORM SEAL CAVITY ANALYSIS	KEETON/LOWRY DATE NOVEMBER 1984

BASELINE SEAL CONFIGURATION WITH AVERAGE TURBINE DISCHARGE PRESSURE

CFD GRID

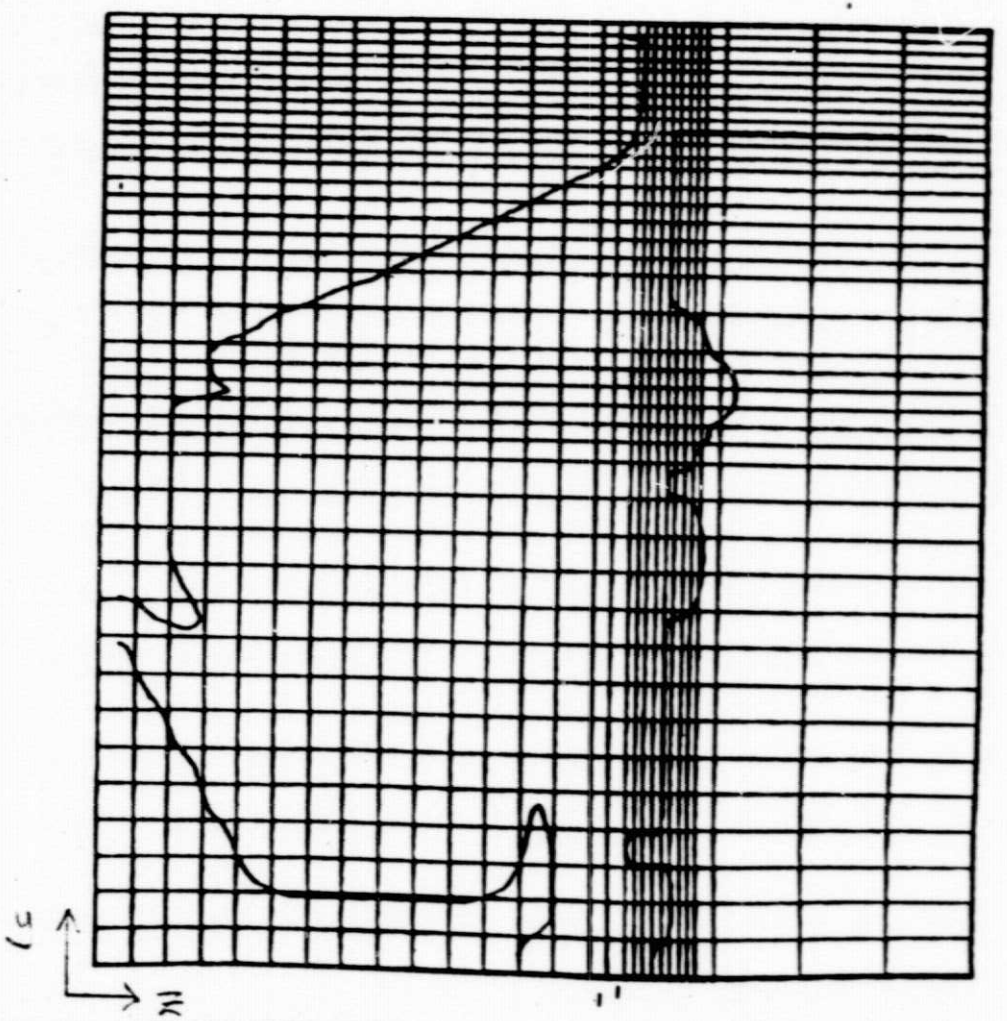

Figure 3

ORGANIZATION	MARSHALL SPACE FLIGHT CENTER	NAME.
CHAM/NASA	SSME HIGH PRESSURE FUEL PUMP AFT PLATFORM SEAL CAVITY ANALYSIS	KEETON/LOWRY DATE. NOVEMBER 1984

BASELINE SEAL CONFIGURATION WITH AVERAGE TURBINE DISCHARGE PRESSURE

VELOCITY VECTORS & STREAMLINES

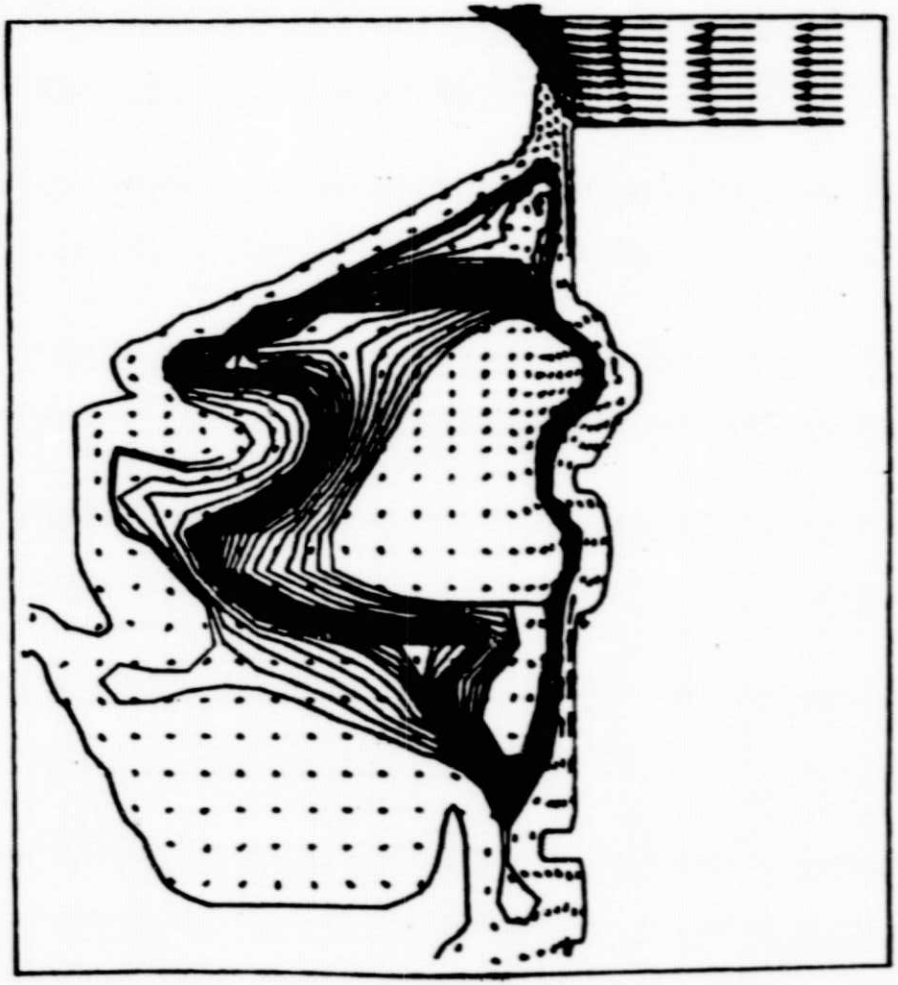

Figure 4

FILE NO 8

ORGANIZATION	MARSHALL SPACE FLIGHT CENTER	NAME
CHAM/NASA	SSME HIGH PRESSURE FUEL PUMP AFT PLATFORM SEAL CAVITY ANALYSIS	KEETON/LOWRY DATE NOVEMBER 1984

BASELINE SEAL CONFIGURATION WITH AVERAGE TURBINE DISCHARGE PRESSURE

VELOCITY VECTORS & STREAMLINES

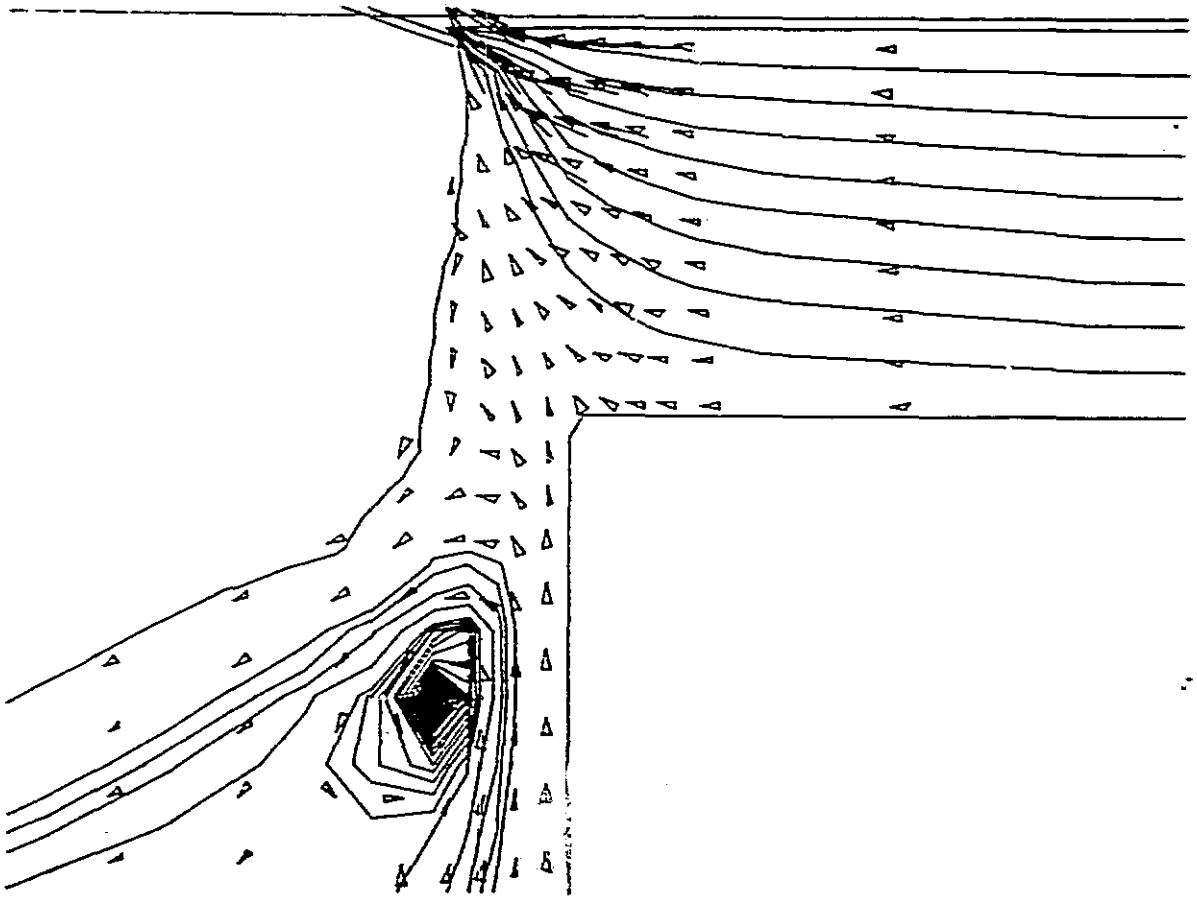

Figure 5

ORGANIZATION:	MARSHALL SPACE FLIGHT CENTER	NAME:
CHAM/NASA	SSME HIGH PRESSURE FUEL PUMP AFT PLATFORM SEAL CAVITY ANALYSIS	KEETON/LOWRY DATE: NOVEMBER 1984

BASELINE SEAL CONFIGURATION WITH AVERAGE TURBINE DISCHARGE PRESSURE

CONSTANT
TEMPERATURE LINES

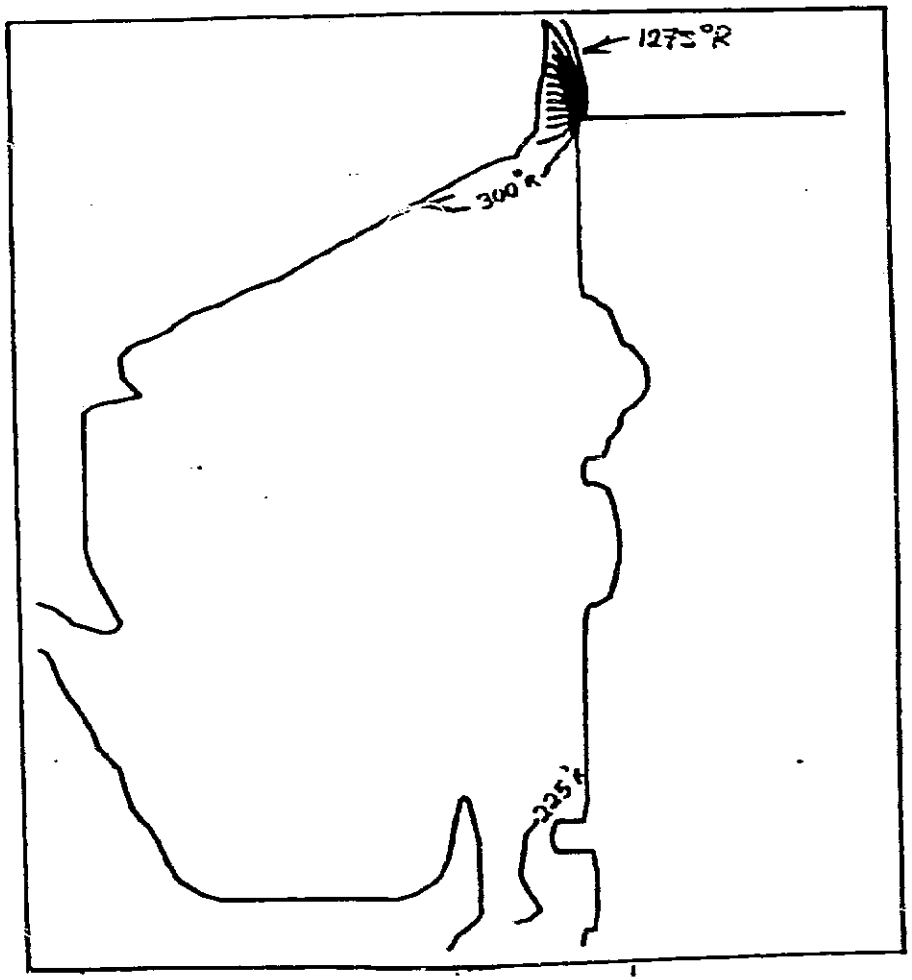

Figure 6

ORGANIZATION	MARSHALL SPACE FLIGHT CENTER	NAME
CHAM/NASA	SSME HIGH PRESSURE FUEL PUMP AFT PLATFORM SEAL CAVITY ANALYSIS	KEETON/LOWRY DATE NOVEMBER 1984

BASELINE SEAL CONFIGURATION WITH AVERAGE TURBINE DISCHARGE PRESSURE

CONSTANT
CONCENTARTION LINES
MASS RATIO OF H_2O

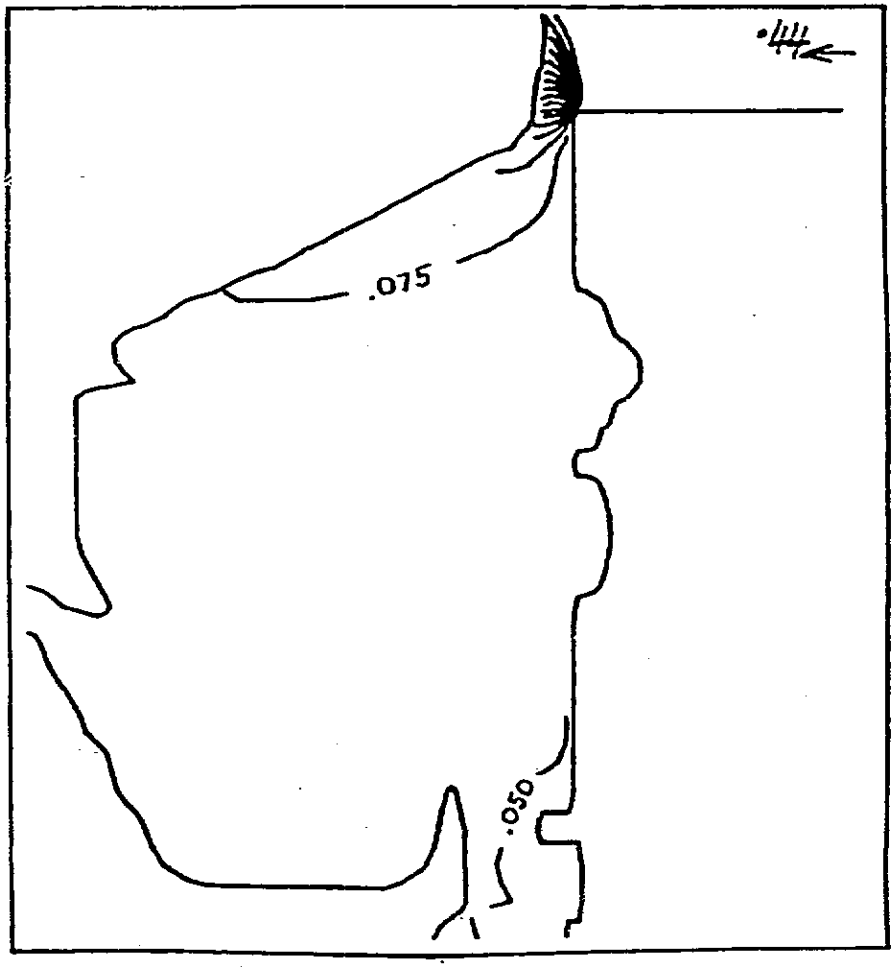

Figure 7

ORGANIZATION	MARSHALL SPACE FLIGHT CENTER	NAME:
CHAM/NASA	SSME HIGH PRESSURE FUEL PUMP AFT PLATFORM SEAL CAVITY ANALYSIS	KEETON/LOWRY DATE: NOVEMBER 1984

BASELINE SEAL CONFIGURATION WITH AVERAGE TURBINE DISCHAGE PRESSURE

ISOBARS: STATIC PRESSURE

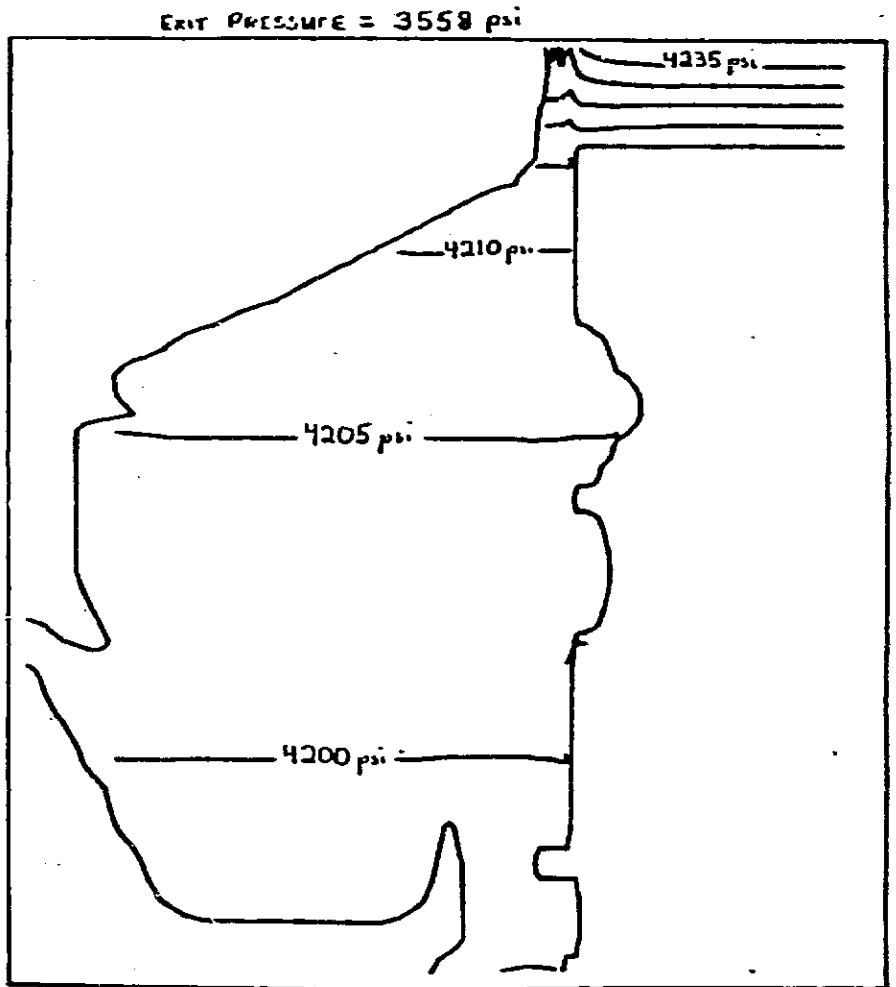

Figure 8

ORGANIZATION	MARSHALL SPACE FLIGHT CENTER	NAME.
CHAM/NASA	SSME HIGH PRESSURE FUEL PUMP AFT PLATFORM SEAL CAVITY ANALYSIS	KEETON/LOWRY DATE. NOVEMBER 1984

MODIFIED SEAL CONFIGURATION (HOLE IN AFT PLATFORM SEAL)

360^{0} AREA OF HOLE = .307 SQ. IN.

VELOCITY VECTORS &
STREAMLINES

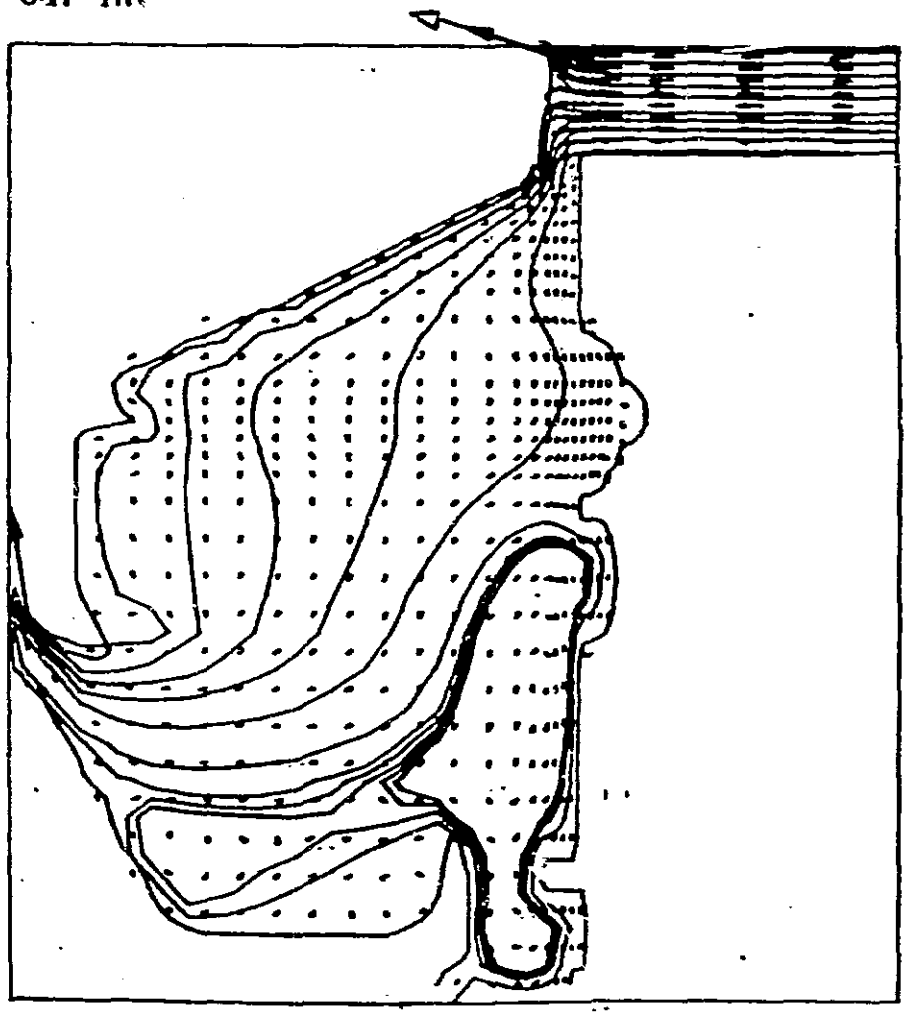

Figure 9

ORGANIZATION:	MARSHALL SPACE FLIGHT CENTER	NAME:
CHAM/NASA	SSME HIGH PRESSURE FUEL PUMP AFT PLATFORM SEAL CAVITY ANALYSIS	KEETON/LOWRY DATE: NOVEMBER 1984

MODIFIED SEAL CONFIGURATION (HOLE IN AFT PLATFORM SEAL)

360^{0} AREA OF HOLE = .307 SQ. IN.

VELOCITY VECTORS & STREAMLINES

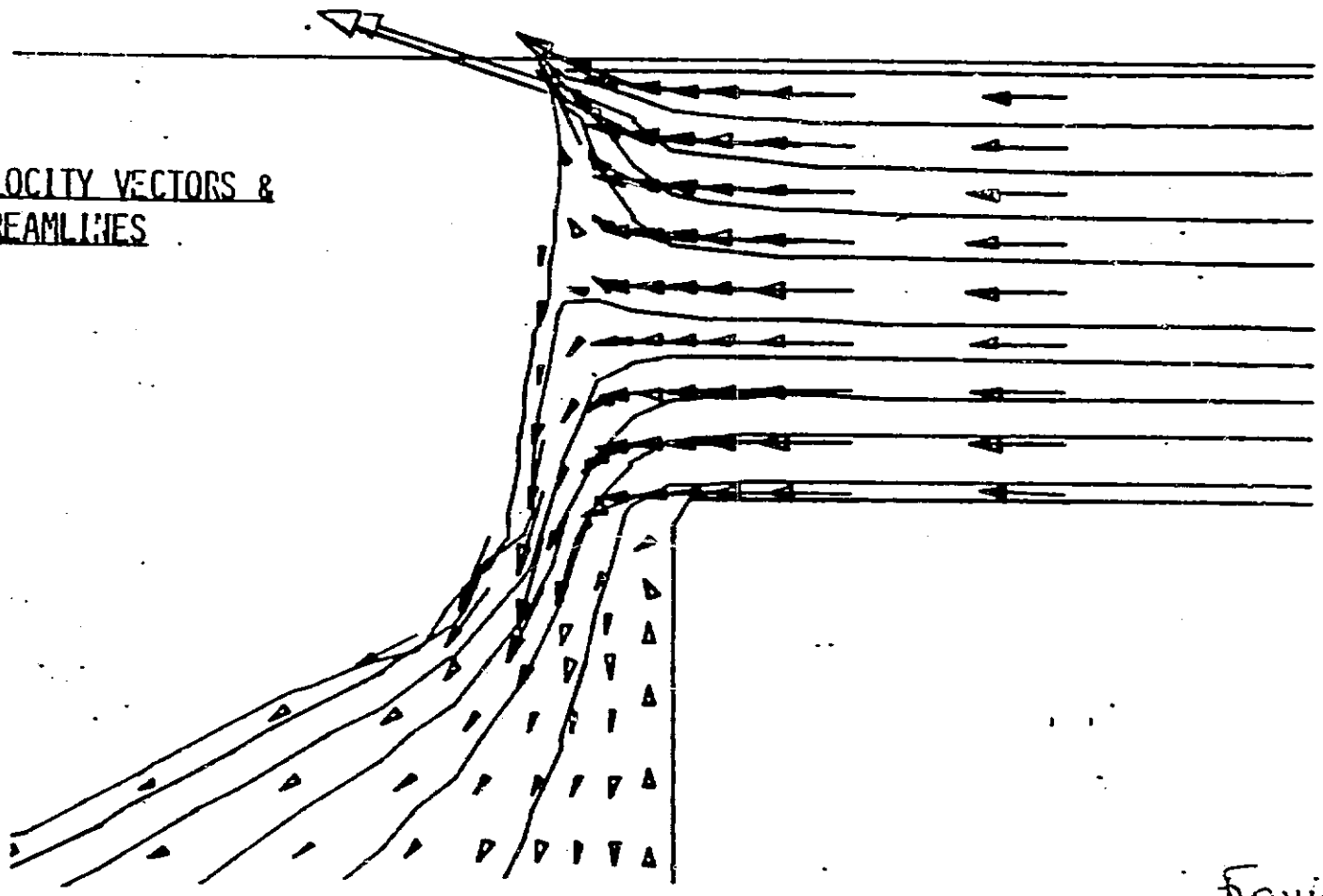

Figure 10

ORGANIZATION:	MARSHALL SPACE FLIGHT CENTER	NAME:
CHAM/NASA	SSME HIGH PRESSURE FUEL PUMP AFT PLATFORM SEAL CAVITY ANALYSIS	KEETON/LOWRY DATE: NOVEMBER 1984

MODIFIED SEAL CONFIGURATION (HOLE IN AFT PLATFORM SEAL)

360^0 AREA OF HOLE = .307 SQ. IN.

CONSTANT TEMPERATURE LINES

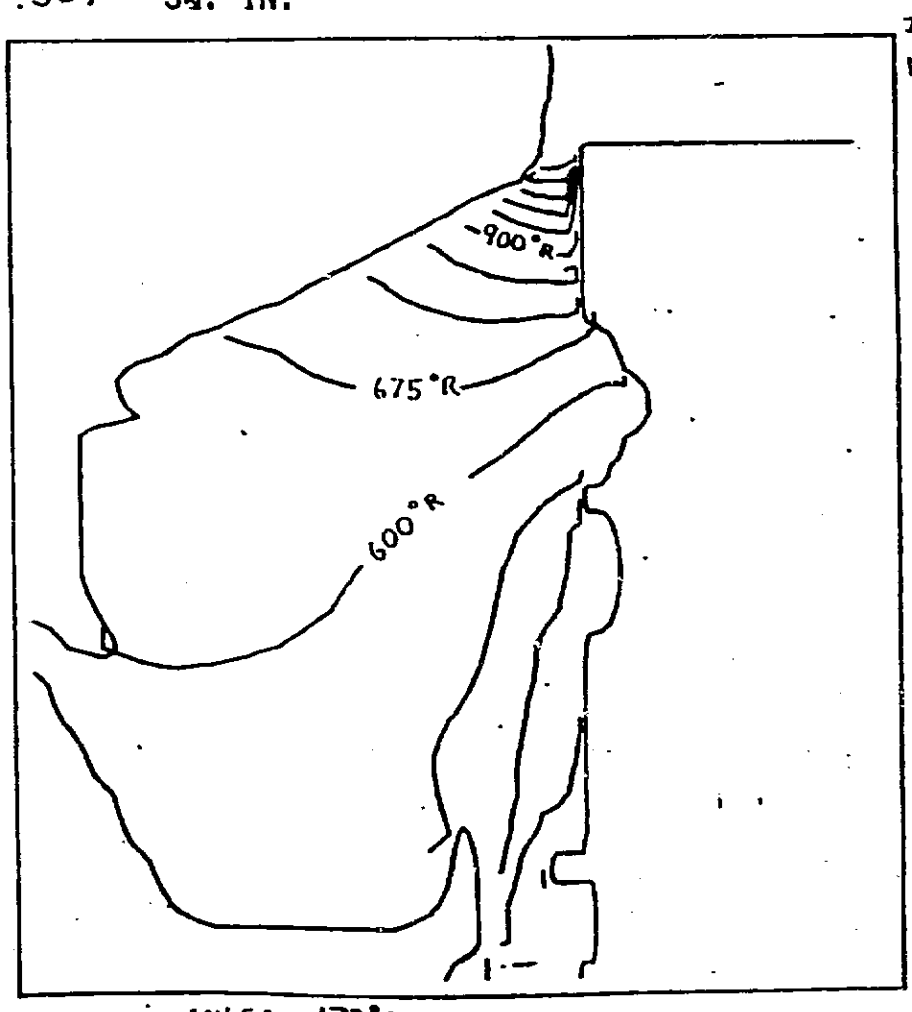

Figure 11

FILE NO

ORGANIZATION:	MARSHALL SPACE FLIGHT CENTER	NAME:
CHAM/NASA	SSME HIGH PRESSURE FUEL PUMP AFT PLATFORM SEAL CAVITY ANALYSIS	KEETON/LOWRY
		DATE: NOVEMBER 1984

MODIFIED SEAL CONFIGURATION (HOLE IN AFT PLATFORM SEAL)

360^{0} AREA OF HOLE = .0102 SQ. IN.

VELOCITY VECTORS & STREAMLINES

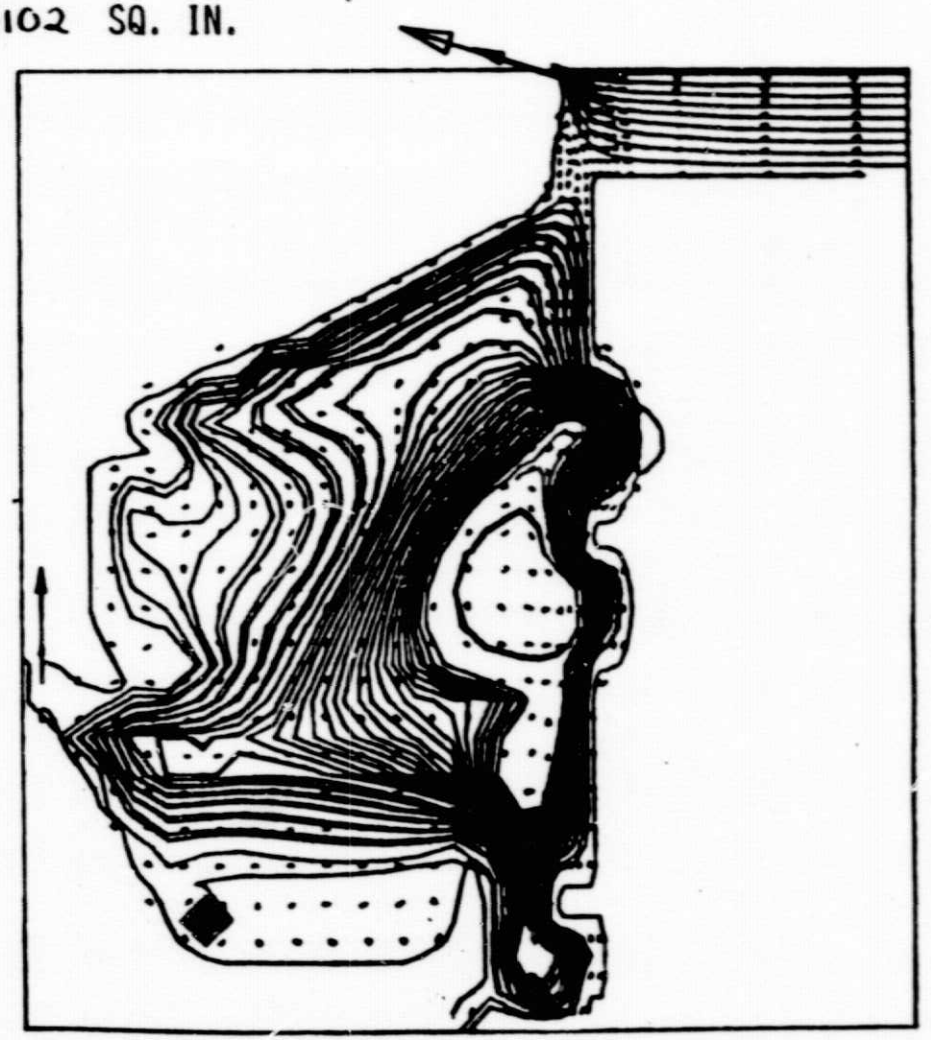

Figure 12

FILE NO.

ORGANIZATION.	MARSHALL SPACE FLIGHT CENTER	NAME.
CHAM/NASA	SSME HIGH PRESSURE FUEL PUMP AFT PLATFORM SEAL CAVITY ANALYSIS	KEETON/LOWRY DATE. NOVEMBER 1984

MODIFIED SEAL CONFIGURATION (HOLE IN AFT PLATFORM SEAL)

360° AREA OF HOLE = .0102 SQ. IN.

VELOCITY VECTORS & STREAMLINES

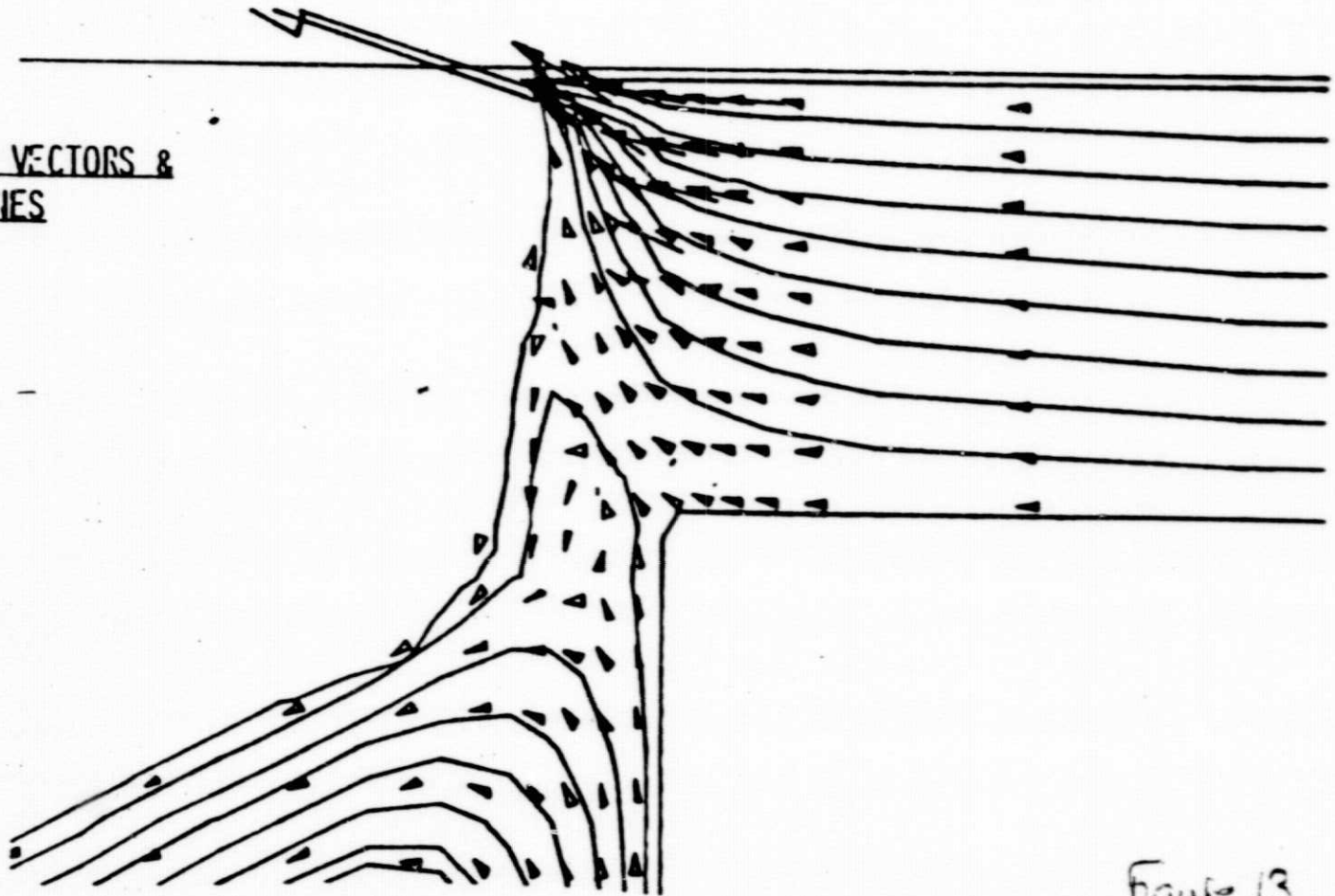

Figure 13

ORGANIZATION:	MARSHALL SPACE FLIGHT CENTER	NAME:
CHAM/NASA	SSME HIGH PRESSURE FUEL PUMP AFT PLATFORM SEAL CAVITY ANALYSIS	KEETON/LOWRY DATE: NOVEMBER 1984

MODIFIED SEAL CONFIGURATION (HOLE IN AFT PLATFORM SEAL)

360^0 AREA OF HOLE = .0102 SQ. IN.

CONSTANT TEMPERATURE LINES

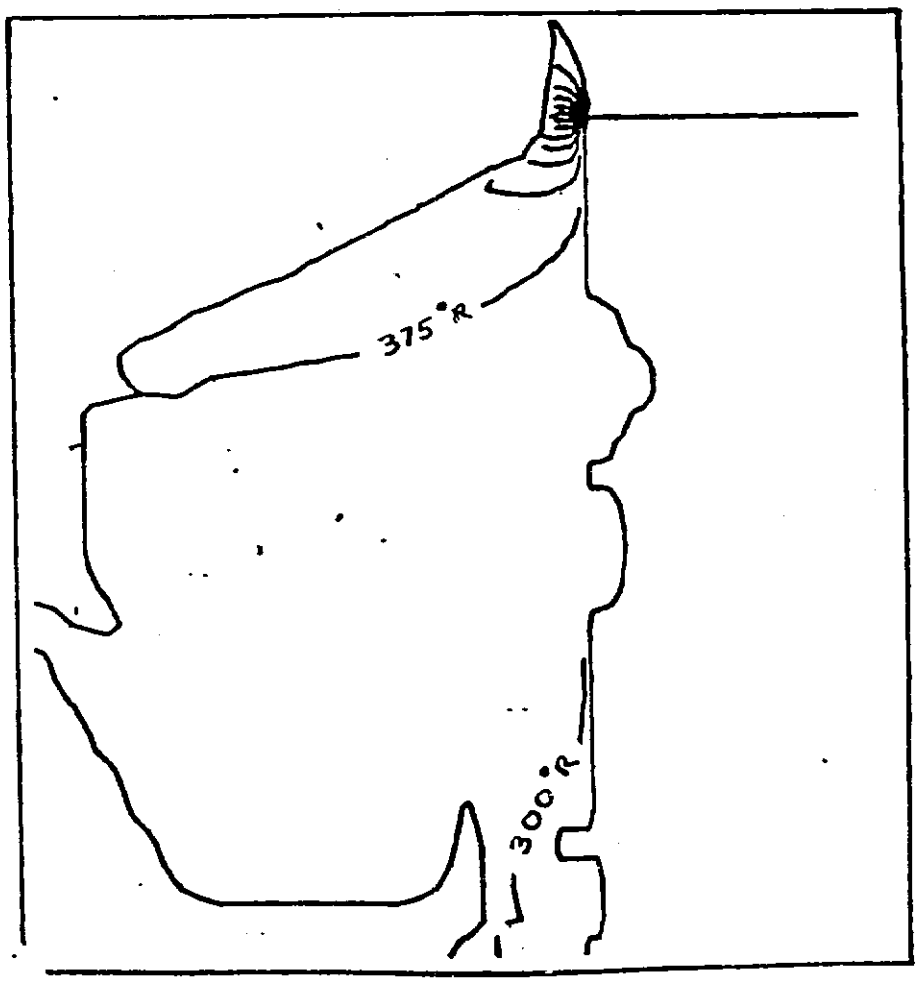

Figure 14

FAS NO. 15

APPENDIX A

Property Curve Fits Used for SSME HPFTP Analysis

In the following pages the curve fit data used in the HPFTP aft-platform seal model for enthalpy, density and viscosity of both water and hydrogen are given in both numerical (equations) and graphical form. The pressure at which these have all been evaluated is approximately 4000 psi.

References for each set of data are included with each curve fit.

ENTHALPY OF WATER[1]

CURVE FIT I $(492 \leq T < 975R)$ $\quad H\ (Btu/lbm) = -424.5938 + .82414T + 1.3067 \times 10^{-4} T^2$

CURVE FIT II $(975R \leq T < 1184.6R)$ $\quad H = 2289.552 - 4.577089T + 2.815249 \times 10^{-3} T^2$

CURVE FIT III $(1184.6R \leq T < 1223.3R)$ $\quad H = -7363.69 + 6.913T$

CURVE FIT IV $(1223.3R \leq T < 1281.4R)$ $\quad H = 599.5881 - 1.27177T + 1.369267 \times 10^{-3} T^2$

CURVE FIT V $(1281.4R \leq T \leq 1400R)$ $\quad H = -307.5449 + 1.190721T$

STANDARD ERROR = 4.08 Btu/lbm

[1]These curves were fit to data taken from Thermodynamic Properties of Steam, Joseph Keenan and Frederick Keyes, (New York: Wiley and Sons, 1936) pp. 72-75.

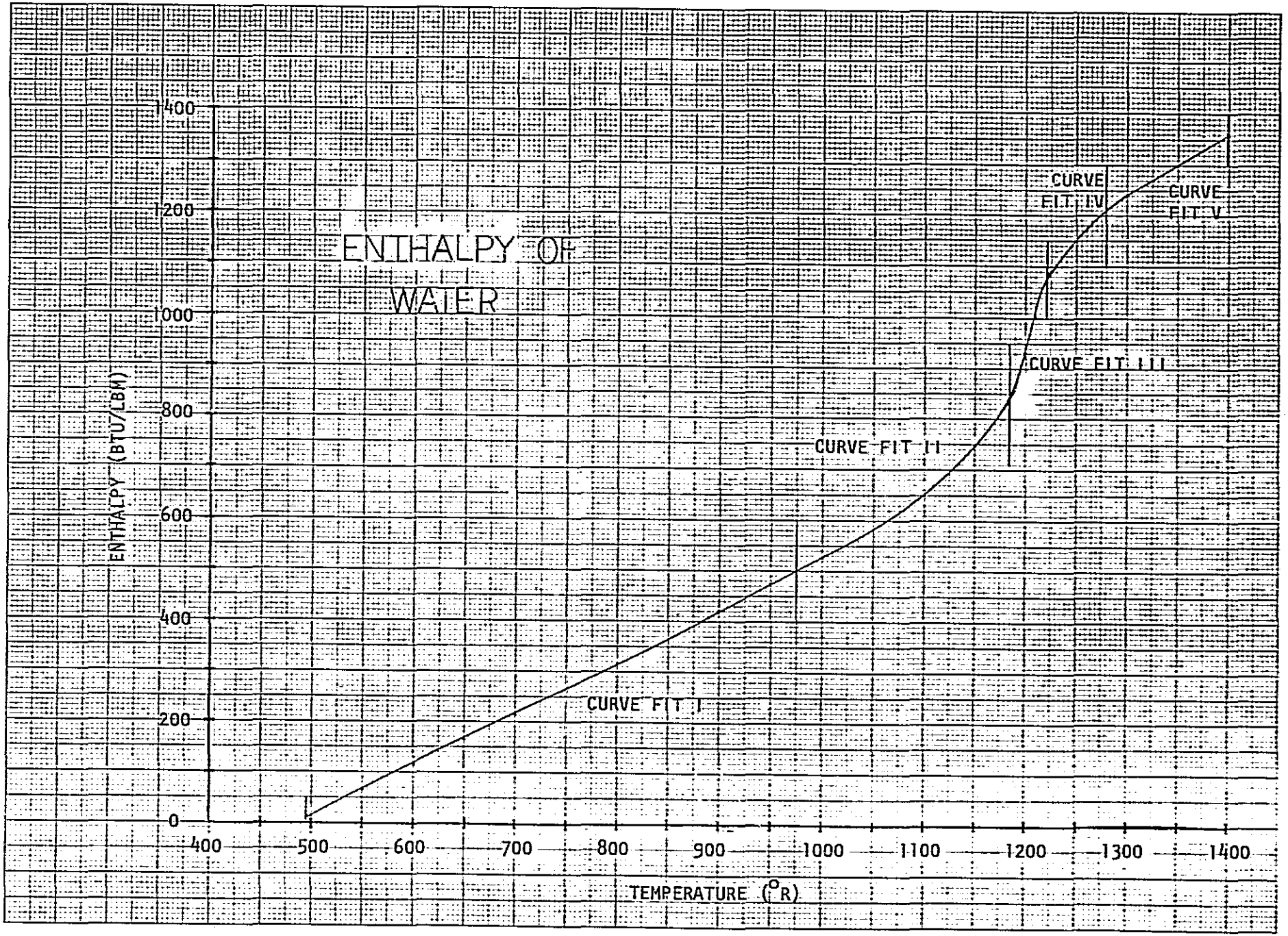
ENTHALPY OF WATER
CURVE FIT I
CURVE FIT II
CURVE FIT III
CURVE FIT IV
CURVE FIT V
ENTHALPY (BTU/LBM)
0
200
400
600
800
1000
1200
1400
400
500
600
700
800
900
1000
1100
1200
1300
1400
TEMPERATURE (°R)

DENSITY OF WATER[2]

CURVE FIT I
($490R \leq T < 1180R$)

$$\text{density } (lbm/ft^3) = -82.117 + .62353T - 6.77693\times10^{-4}T^2 - 3.41207\times10^{-7}T^3 + 9.23406\times10^{-10}T^4 - 3.9688\times10^{-13}T^5$$

CURVE FIT II
($1180R \leq T < 1250R$)

$$\text{density} = -2177.783 + 7.12733T - 4.54395\times10^{-3}T^2 - 1.91391\times10^{-6}T^3 + 1.686\times10^{-9}T^4$$

CURVE FIT III
($1250R \leq T \leq 1400R$)

$$\text{density} = 119.1372 - 4.770357\times10^{-2}T - 1.00694\times10^{-4}T^2 + 5.516186\times10^{-8}T^3$$

STANDARD ERROR = 0.61 lbm/ft^3

[2]These curves are fit to data taken from Keenan, pp. 72-75.

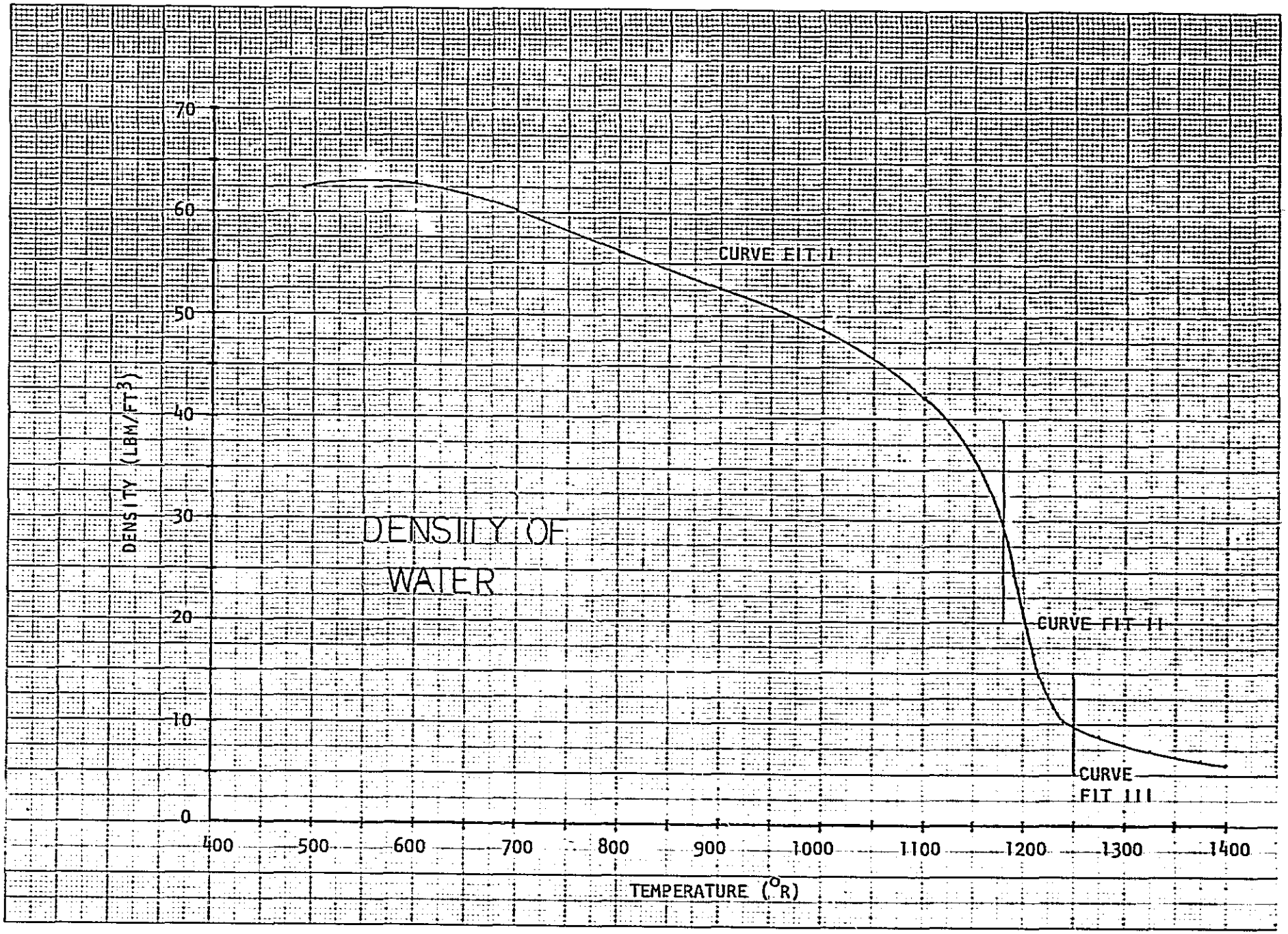
DENSITY OF WATER
DENSITY (LBM/FT³)
70
60
50
40
30
20
10
0
400
500
600
700
800
900
1000
1100
1200
1300
1400
TEMPERATURE (°R)
CURVE FIT I
CURVE FIT II
CURVE FIT III

VISCOSITY OF WATER[3]

$$\text{VISC } (\times 10^3) = e^{\left[\begin{array}{l} 20.5532 - 6.52199\times10^{-2}T + 3.2726\times10^{-5}T^2 \\ + 6.6687\times10^{-8}T^3 - 8.3627\times10^{-11}T^4 + 2.6237\times10^{-14}T^5 \end{array}\right]}$$

$$\text{STANDARD ERROR } (\times 10^3) = 0.0066 \text{ lb/ft-sec}$$

[3]This curve is fit to data taken from Steam Tables, Joseph Keenan, et al., (New York: Wiley and Sons, Inc., 1969) p. 113.

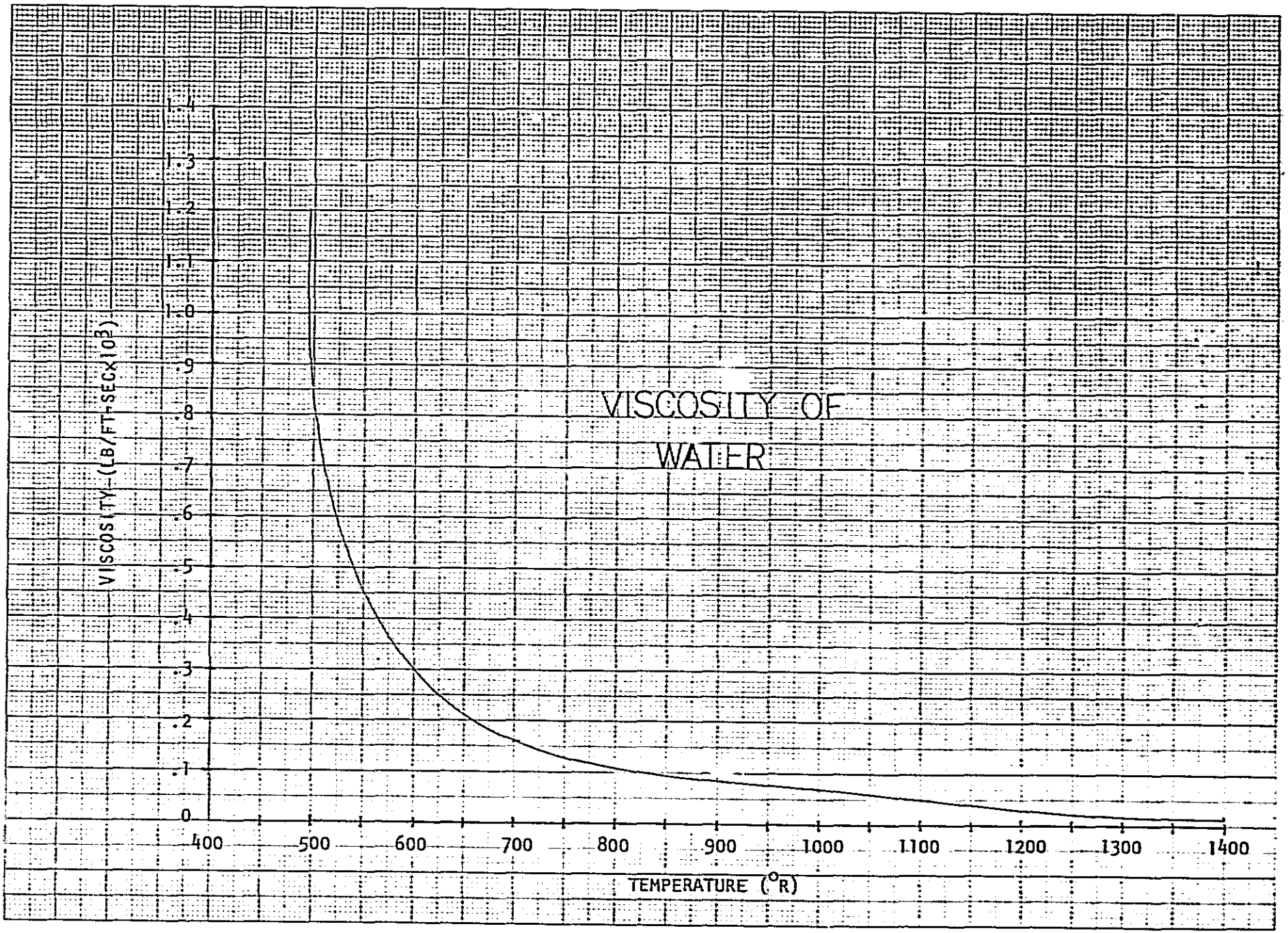

ENTHALPY OF HYDROGEN[4]

CURVE FIT I
(170R≤T≤508R) $H\ (Btu/lbm) = -5.92706 \times 10^{-4} T^2 + 4.468995T - 357.6903$

CURVE FIT II
(508R<T≤2000R) $H = -7.15694 \times 10^{-6} T^2 + 3.557702T - 45.88906$

STANDARD ERROR = 4.39 Btu/lbm

[4]These curves are fit to data taken from the Hydrogen Technological Survey - Thermophysical Properties, Robert D. McCarty, (Washington, D.C.: NASA Scientific and Technical Information Office, 1975) p. 472.

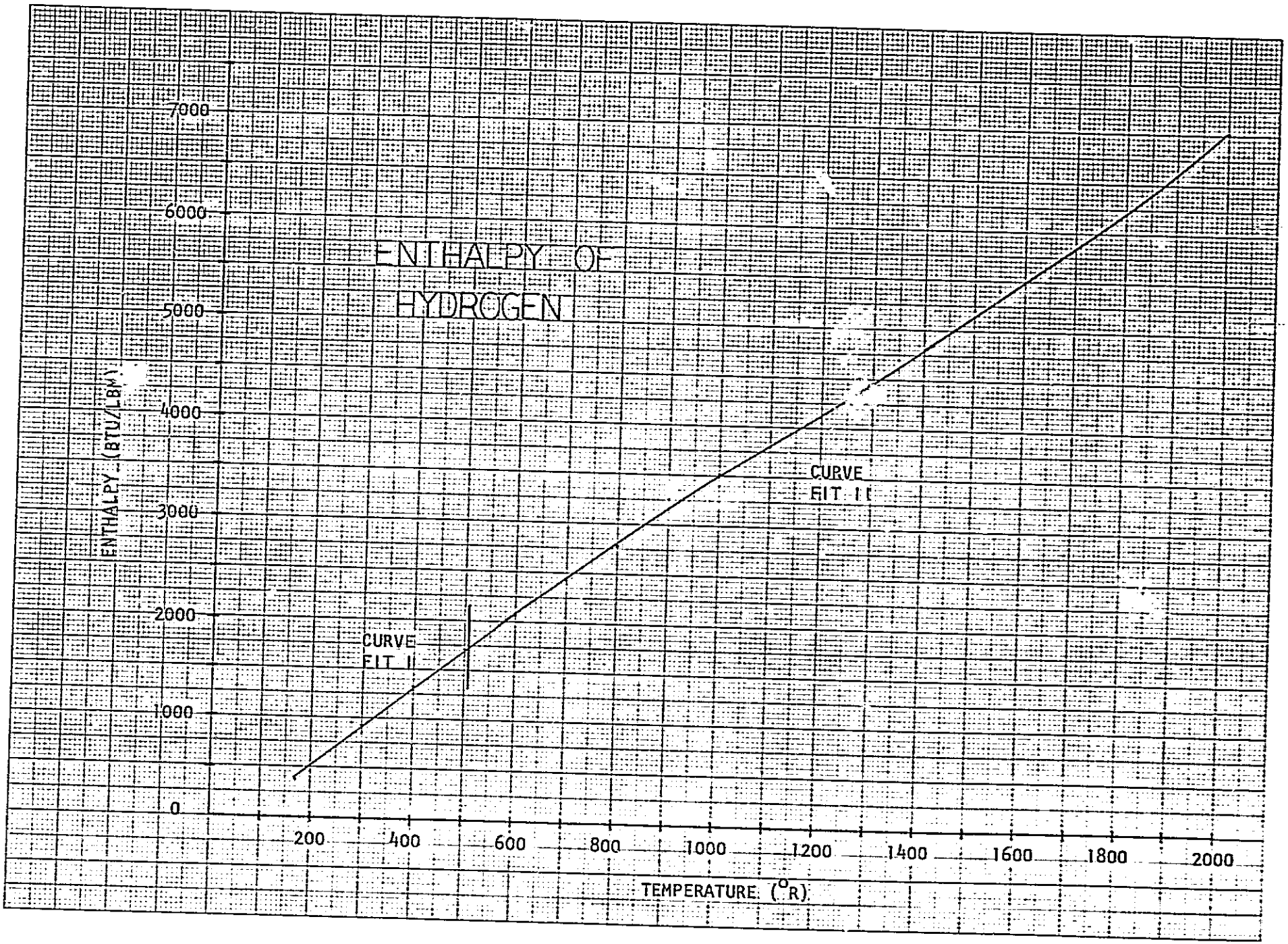
ENTHALPY OF HYDROGEN
ENTHALPY - (BTU/LBM)
7000
6000
5000
4000
3000
2000
1000
0
200
400
600
800
1000
1200
1400
1600
1800
2000
TEMPERATURE (°R)
CURVE FIT I
CURVE FIT II

DENSITY OF HYDROGEN[5]

$$\text{density } (\text{lbm/ft}^3) = e^{\left[\begin{array}{l} -5.26685 + 3.049183(\ln H) - .41497(\ln H)^2 \\ + 1.40759\times10^{-2}(\ln H)^3 \end{array}\right]}$$

where H is the enthalpy of hydrogen.

STANDARD ERROR = .0189 lbm/ft^3

[5]This curve is fit to data taken from McCarty, p. 472.

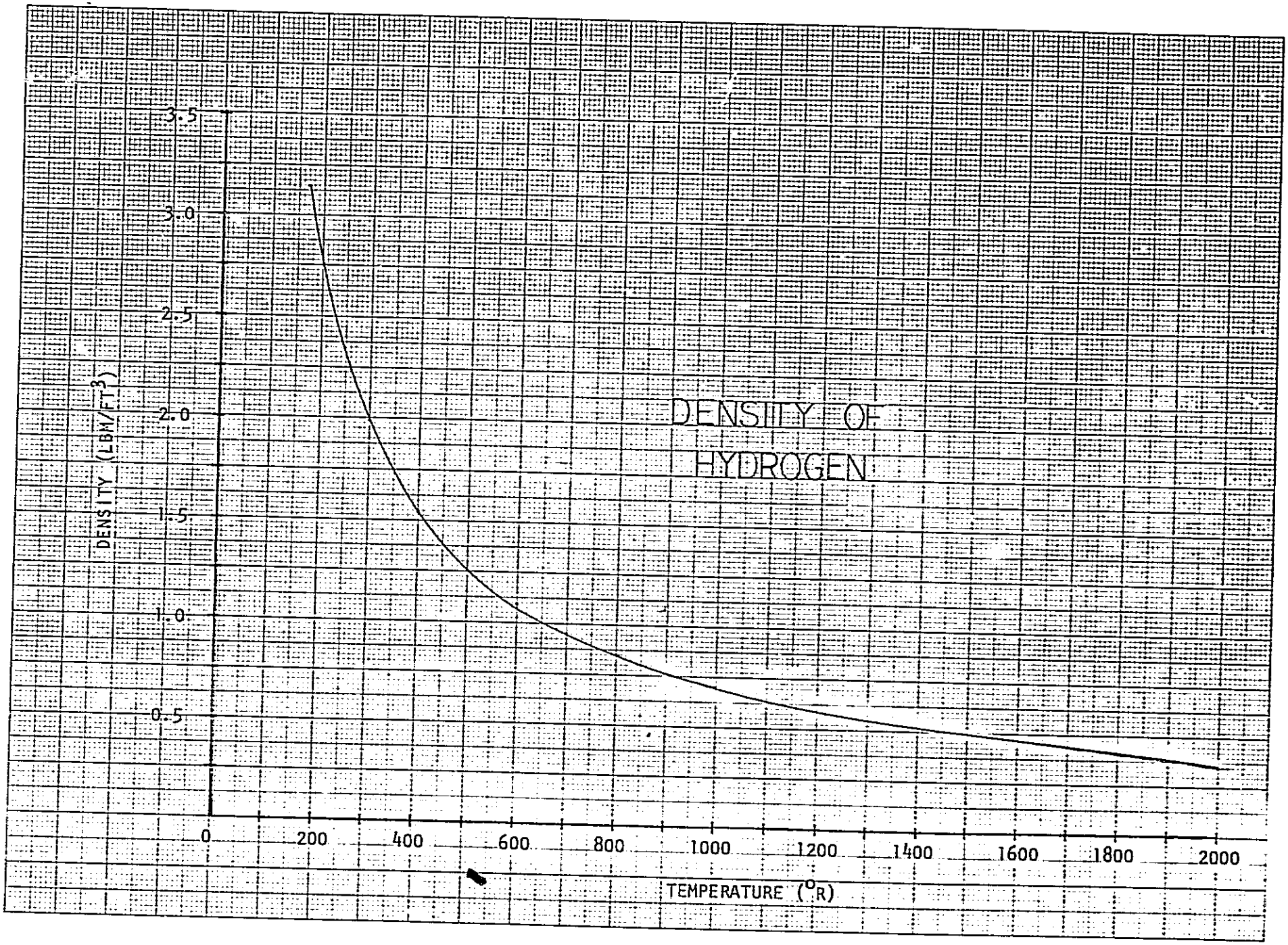
DENSITY OF HYDROGEN
DENSITY (LBM/FT^3)
3.5
3.0
2.5
2.0
1.5
1.0
0.5
0
200
400
600
800
1000
1200
1400
1600
1800
2000
TEMPERATURE ($^\circ$R)

VISCOSITY OF HYDROGEN[6]

$$\text{VISC. (lbm/ft-sec } \times 10^5) = .4989 - 5.4575\times10^{-5}T + 5.1824\times10^{-7}T^2 - 1.4948\times10^{-10}T^3$$

STANDARD ERROR ($\times10^5$) = 0.00047 lbm/ft-sec

[6]This curve is fit to data taken from the Hydrogen Technological Survey - Thermophysical Properties, Robert D. McCarty, (Washington, D.C.: Scientific and Technical Information Office, NASA, 1975) p. 473.

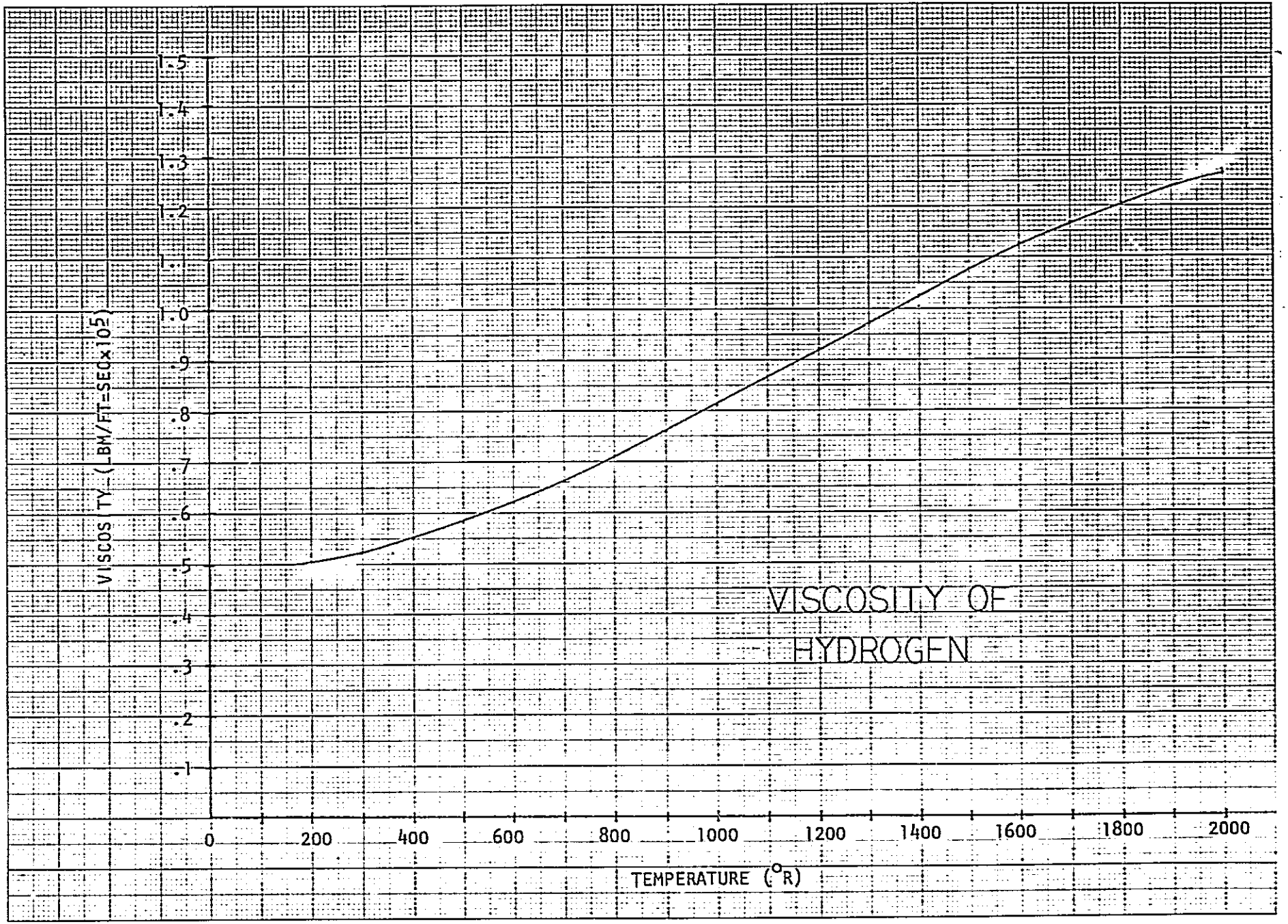

CHAM

APPENDIX 2

Interim Report on

Single-Phase Multi-Component Flow Analysis of a Single Oxygen-Hydrogen Jet of the SSME Preburner

by

C. Prakash and A.K. Singhal

1. ABSTRACT

To further understand the mixing and combustion processes in the SSME fuelside preburner, single oxygen-hydrogen jet element has been investigated. The analysis involves the numerical integration of the governing differential equations. Multicomponent single phase theory is employed, with instantaneous reaction assumed for combustion. Both reacting and non-reacting cases are considered. In the second category (viz: non-reacting cases), one of the case is for the mixing of hydrogen-hydrogen jet.

It is found that the oxygen jet can penetrate a distance of upto 40 jet diameters, which is about 50% of the burner height. Thus, the jets do not necessarily mix in a short distance near the inlet. By comparing the behaviour of the oxygen-hydrogen and hydrogen-hydrogen jets, it is confirmed that the greater penetration in the former case is due to the density difference between oxygen and hydrogen. These results justify the rationale of the two fluid approach for modeling the burner.

A region of recirculating flow is found adjacent to the jets near the inlet. For the combustion case, the temperature distribution shows the expected flame like structure with local regions of very high temperature. Turbulent diffusion is computed using the k-ε model and the effective turbulent viscosity is found to be 10^3 - 10^4 times the laminar value. Sensitivity of the solution to the inlet turbulent kinetic energy is examined. The grid employed was decided upon after a careful grid refinement study.

Having summarised the essential findings, we now proceed with a detailed discussion of the problem description, solution methodology, and the results.

2. THE PROBLEM DESCRIPTION

2.1 Geometry

The problem analysed is schematically sketched in Figure 1. It concerns the prediction of flow and heat transfer due to an element of coaxial oxygen-hydrogen jets. The actual SSME preburner contains 264 such elements. Each element consists of an inner tube of 0.09" diameter which carries the oxygen jet. Concentric with this is an outer tube of 0.154" diameter and hydrogen

flows in through the annular gap. For brevity, the abbreviations O_2 and H_2 (or even O2 and H2 in computer drawn figures) shall be used to refer to oxygen and hydrogen respectively.

The 264 elements in the burner are distributed on a top plate of radius 5.24". The plate area associated with each element is therefore = π $(5.24)^2/264$ = 0.327 sq. in., which is equal to the area of circle of diameter = 0.645". Thus, as shown in Figure 1, we have a symmetry surface of diameter 0.645" around the jets. In the axial direction, the distance of 6.66" corresponds to the distance from the top plate to the turbine dome top in the burner. The distance 2.04" is equal to one half of the distance from the dome top to the exit to the turbine. The outer symmetry surface extends from the inlet to a distance of 6.66"; from thereon, in a further distance of 2.04", the flow is assumed to turn and exit. The wall on the right hand may be taken to simulate the presence of the solid turbine dome. The region adjacent to the jets at the inlet is also a solid wall.

2.2 Property Data

Oxygen

Inlet velocity = 27.96 m/s
Inlet density = 1275.19 kg/m^3
Inlet temperature = 108.32 ^oK
Specific heat = 1004.88 J/(kg. ^oK)

Hydrogen

Inlet velocity = 306.36 m/s
Inlet density = 57.57 kg/m^3
Inlet temperature = 149.69 ^oK
Specific heat = 14612 J/(kg. ^oK)

Water (The Combustion Product)

Specific heat = 2030.7 J/kg ^oK

Other data

Heat of combustion = 1.7974×10^7 J/(per kg of oxygen)
Pressure at exit = 352 psi = 352×10^5 N/m^2.

2.3 The Model Employed/Fluid Properties

The present study employs a multicomponent single-phase model - there is no two fluid model involved here. The components in the fluid are: oxygen, hydrogen and water (combustion product). Each component is characterised by its concentration. Temperature is obtained from enthalpy using an average specific heat for the mixture. The density of the mixture fluid is obtained by using the mixture temperature and ideal gas law with the partial pressure procedure.

2.4 The Turbulence Model

The k$\omega\varepsilon$ model was used to compute turbulent diffusion. The following data was employed:

Laminar Viscosity $\mu_{\ell am} = 10^{-5}$ kg/m s

Turbulent Prandtl number, $\sigma_t = 1$

Turbulent Schmidt number, $\sigma_c = 1$

Inlet velocity fluctuations due to turbulence = 5% of mean flow hence, turbulence kinetic energy at the inlet, k_{in} = .0025 x (kinetic energy of mean flow)

Dissipation rate ε at the inlet, $\varepsilon_{in} = 0.164\ k_{in}^{3/2}/\ell$ where ℓ is a mixing length = 0.09 x some characteristic length. The characteristic length was taken to be = 0.1" which is ≃ inlet oxygen jet diameter.

The turbulent viscosity, μ_{eff}, is determined from k and ε. For the energy or the species concentration equation, the diffusion coefficient is taken to be μ_{eff}/σ where σ is the turbulent Prandtl (or Schmidt) number. The value of laminar viscosity is required since wall functions are invoked to compute the shear stresses near the walls. The walls are taken to be impervious to heat or any species concentration; hence, no wall treatment is necessary, and the values of laminar Prandtl or Schmidt number are therefore not required.

2.5 The Combustion Model

The reaction is assumed to be instantaneous. Thus, at any point, there can either be oxygen, or hydrogen, but not both.

3. MATHEMATICAL FORMULATION

3.1 Equations to be Solved

The problem is governed by partial differential equations - the Navier-Stokes equations - representing the conservation of mass, momentum and energy. Since the problem is axisymmetric, only two velocity components, radial and axial, need to be solved for. Pressure is determined by the continuity constraint. Time averaged form of the governing equations are solved with, as already mentioned, the $k\text{-}\varepsilon$ model employed to compute turbulent diffusion. Both k and ε have their own partial differential equations which are solved as part of the iterative calculation procedure. Since the combustion model assumes instantaneous reaction, only one species concentration needs to be solved for. A good practice, and the one followed here, is to solve for a suitability defined mixture fraction for which the governing equation is source free.

3.2 Boundary Conditions

At the inlet, all jet properties are known as stipulated earlier. At the symmetry surface (see Figure 1), the normal velocity, and the normal flux of all other variables is zero. The walls are adiabatic and impervious to any species, and the shear stresses are computed using the wall functions. At the section marked exit, the pressure is specified to be equal to 352 psi which corresponds, in the actual preburner to the pressure at the turbine inlet.

4. COMPUTATIONAL PROCEDURE/GRID LAYOUT

The PHOENICS code was used in this study. It is based on a control volume type finite differential formulation.

A 15 x 35 non-uniform grid was used in the present investigation. The grid layout is displayed in Figure 2. On any radial grid line, 5 control volumes span the distance equal to the radius of the oxygen jet, 5 control volumes cover the width of the coaxial hydrogen jet, and 5 control volumes cover the remaining space. On any axial line, the first 20 control volumes span a distance equal to 20 oxygen jet diameters. This is followed by 10 control volumes covering the distance upto z = 6.66" (the end of the symmetry surface) and 5 more control volumes span the distance from z = 6.66" to the end wall. This grid size was decided upon after a grid refinement study, results of which are presented in section 5.6.

5. RESULTS

5.1 The Flow Field

The structure of the flow field created by the jets is displayed in Figure 3. where the streamlines have been plotted. Case (a) corresponds to the situation in which the oxygen and hydrogen jets do not react - i.e. when there is no combustion. Case (b) corresponds to a reacting case.

As expexted, a flow recirculation zone exists near the inlet. This is followed by a region in which the flow is primarily in the axial direction.

The difference in the size of the recirculating zones for the reacting and non-reacting cases is to be noted. In the reacting case, the recirculation zone extends till about 18 oxygen jet diameters; for the reacting case, this distance is only about 6 oxygen diameters. This result can be explained by noting that the temperatures are higher and, consequently, the density lower in the combusting case. A smaller value of the density implies a lower inertia, and hence, a smaller recirculation zone.

5.2 Distribution of Oxygen Concentration

Contour levels of oxygen concentration are shown in Figure 4. Consider the reacting case first. It shows a pattern which is typical of fuel distribution in diffusion flames. The "bump" near the inlet is caused by diffusion; further down, the bump disappears, and the region of non-zero oxygen concentration decreases as more of the oxygen gets depleted due to combustion.

For the given data, the total mass flow rate of oxygen and hydrogen into the system is about equal. Hence, in the non-reacting case, the oxygen concentration far from the inlet should be 0.5. This is also seen from Figure 4(a).

In the region close to the wall and the symmetry surface near the inlet (the top-left corner), there is a significant oxygen concentration for the non-reacting case, but zero for the reacting case. This is due to the fact that in the non-reacting case the large recirculating eddy convects oxygen from further downstream into the top left corner. In the reacting case, on the other hand, the recirculating eddy is small as already seen, and, it is confined to a region in which oxygen just cannot reach - i.e. oxygen gets lost due to combustion before being able to diffuse that far.

Further perspective to the oxygen concentration is provided by Figure 5 in which its variation along the jet centerline (r = 0) is plotted. The symbol D02 on the abcissa refers to the oxygen jet diameter at the inlet (=0.09"). In the non-reacting case, the oxygen concentration must decay to 0.5 as already discussed. As can be seen, the oxygen jet penetrates further for the combusting case as compared to the non-reacting situation. This results in also evident from Figure 4. This is due to increased velocities in the combusting case. Another reason for this behavior lies in the level of turbulent diffusion coefficient: as will be discussed in Section 5.4, the k-ε model predicts much lower turbulent diffusion (especially in the flame region) for the reacting case as compared with non-reacting case.

The fact that the oxygen jet can penetrate a distance of upto 40 jet diameters into the burner is important. This distance is about 40 - 50% of the burner height.

5.3 Temperature Distribution

The temperature distribution for the reacting case is shown in Figure 6. It has, as can be seen, a typical flame-like behavior, with local regions of very high temperature. The highest temperature is consistent with the given specific heat and heat of combustion data.

5.4 The Effective Turbulent Viscosity

For this diffusion controlled combustion process, the level of turbulent diffusion is important. Contour plots of the turbulent viscosity are shown in Figure 7. As can be seen, μ_{eff}/μ_{lam} lies in the range of 10^2 - 10^4.

It may be observed that the turbulent diffusion is generally smaller in the combustion case as compared to the non-reacting case. The level of turbulent diffusion is particularly small in the flame region for the combustion case.

The relatively low turbulence levels for the combustion case can be explaned by noting that the flow in this case is characterized by higher temperatures. Hence, the density is smaller, implying smaller inertia forces. As a consequence, the recirculation zone is smaller (recall Figure 3) so that the gradients in the mean velocity are less. This implies a lower dissipation rate in the mean flow which results in smaller values of the turbulent kinetic energy k, and hence smaller values of μ_{eff}.

The sensitivity of the results to the kinetic energy at the inlet is important, and Figure 8 has been prepared to this effect. The base line case is compared to a situation in which k_{in} = 0.05 x mean kinetic energy. As can be seen, the results are, but not extremely, sensitive to the inlet turbulent kinetic energy. The baseline case has a lower k_{in}, and hence, lower μ_{eff} or, smaller diffusion. At any z, the oxygen concentration would, therefore, be greater for the baseline case, and this is also shown by the present computations.

5.5 Effect of Density Difference Between the Jets on the Penetration Depth

An interesting quantity to examine is the effect of density difference between the jets on the penetration depth. For this a special case was considered where oxygen is replaced by another gas which has the same density at the inlet and the same molecular weight as that for the neighboring hydrogen jet. The velocity of the inner jet, however, was the same as that of the baseline oxygen case (= 27.96 m/s). This special case is referred to as the H_2/H_2 case; the original baseline case is called the O_2/H_2 case.

Variation of concentration of the gas in the inner jet is plotted in Figure 9. The results correspond to the centerline, i.e. at r = 0. At z = 0, i.e. the inlet, this concentration is equal to 1. For large axial distance (z) the concentration c must approach c_∞ where c_∞ is the mass fraction of the inner gas in the incoming stream. For the O_2/O_2 case, c_∞ = .504; for the H_2/H_2 case, c_∞ = .044.

As can be seen, the inner jet decays much more rapidly for the H_2/H_2 case. This is understandable: the higher density of oxygen leads to higher inertia (i.e. higher Peclet number) permitting the oxygen jet to penetrate much deeper. The penetration depth of O_2/H_2 case is ≈ 20 jet diameters, while the H_2/H_2 case it is only ≈ 10.

In suggesting the two fluid approach to model the burner, the argument made was precisely that the oxygen jet can penetrate very deep due to the density difference between O_2 and H_2. The results of Figure 9 are supportive of this assertion.

5.6 Grid Refinement

To examine the adequacy of the grid, a case was run using a finer, 20 x 45, grid. Sample results of this run are compared with those of the baseline grid in Figure 10. As can be seen, the agreement is very close assuring that the 15 x 35 grid results are quite accurate.

6. CONCLUSIONS

The present sutdy shows that an oxygen jet can penetrate a distance of upto 40 jet diameters into the preburner before burning out. This distance is about 50% of the burner height. The use of the two fluid approach to model the burner is therefore justified.

7. RECOMMENDATIONS FOR FUTURE WORK

Having justified the rationale of the two-fluid approach, we must return to the task of estimating the exchange coefficients C_M and C_F which appear in the expressions for interphase mass and momentum transfer. As a prerequiste, a closer study of the physics of two turbulent coaxial jets will be necessary. Features like entrainment, hair-pin vortices, etc should be closely examined. This will, hopefully, provide some estimate of the average size of oxygen pockets and the mixing length scales around the pockets. These two quantities are essential for developing any semi-empirical expressions for C_M and C_F.

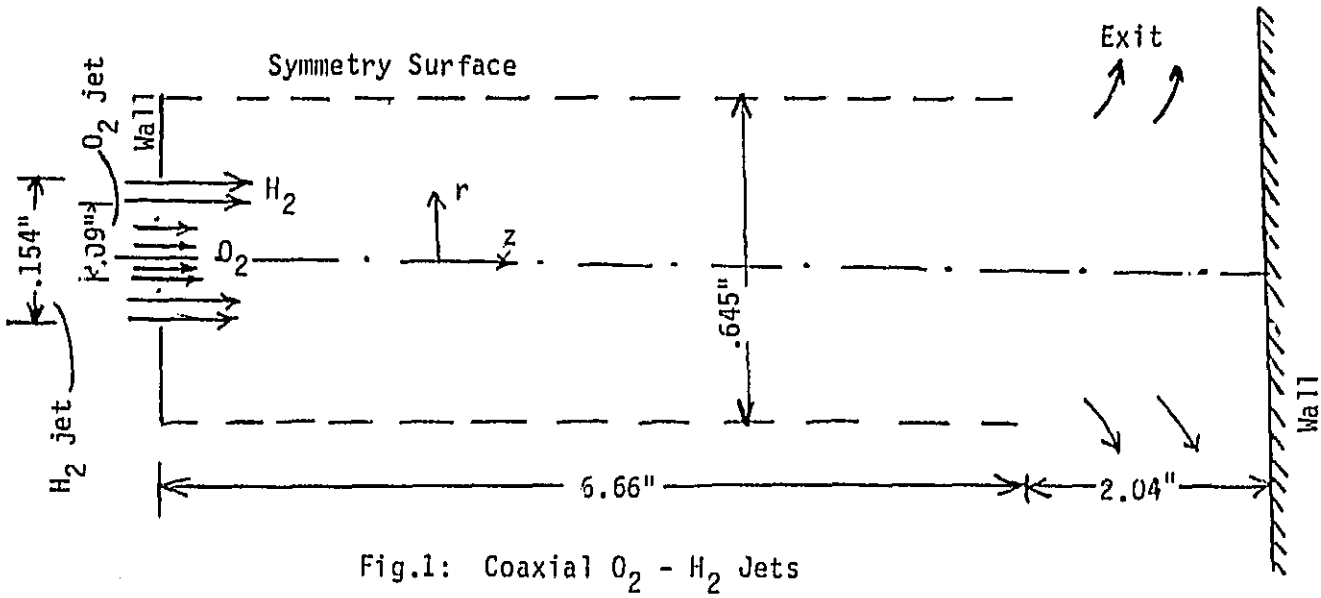

Fig.1: Coaxial O_2 - H_2 Jets

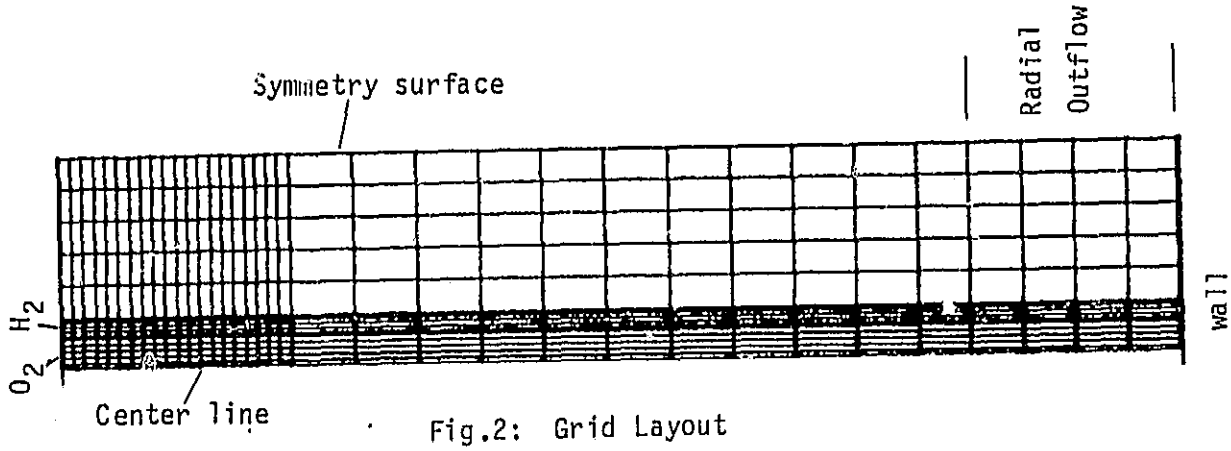

Fig.2: Grid Layout

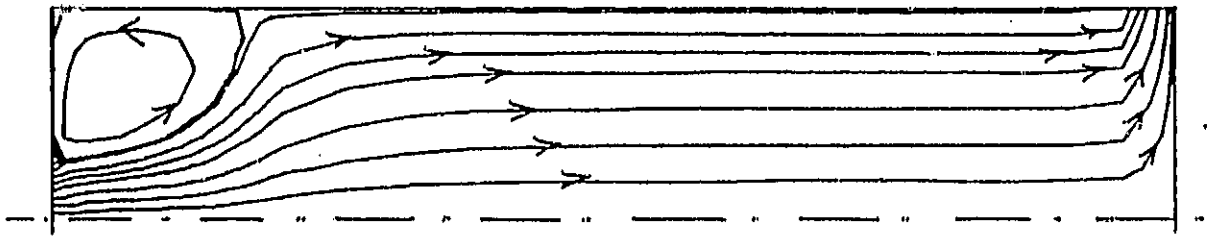

(a) No Combustion

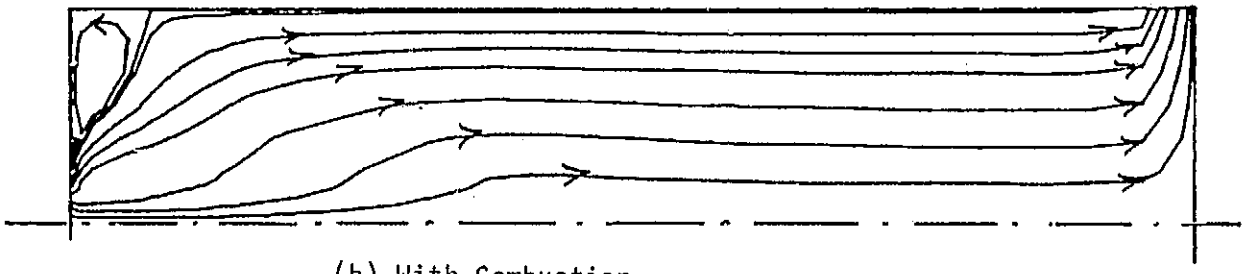

(b) With Combustion

Fig.3: Flow Field/Stream Line Map

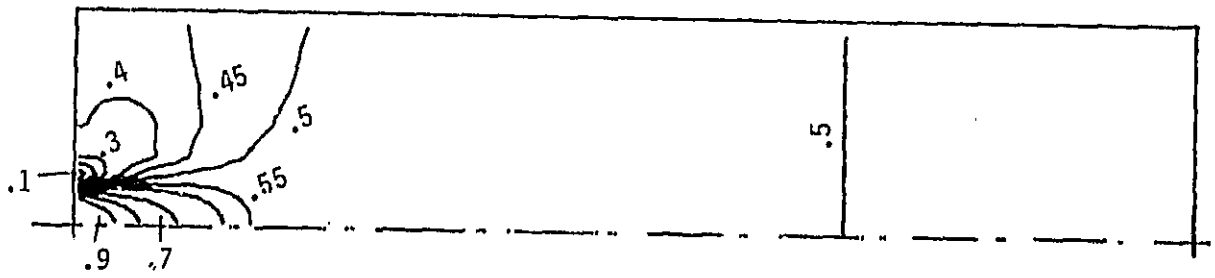

(a) No Combustion

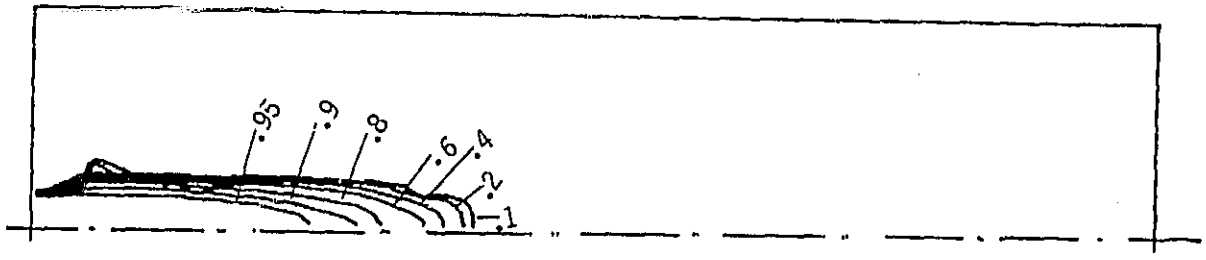

(b) With Combustion

Fig.4: Contour Levels of O_2 concentration

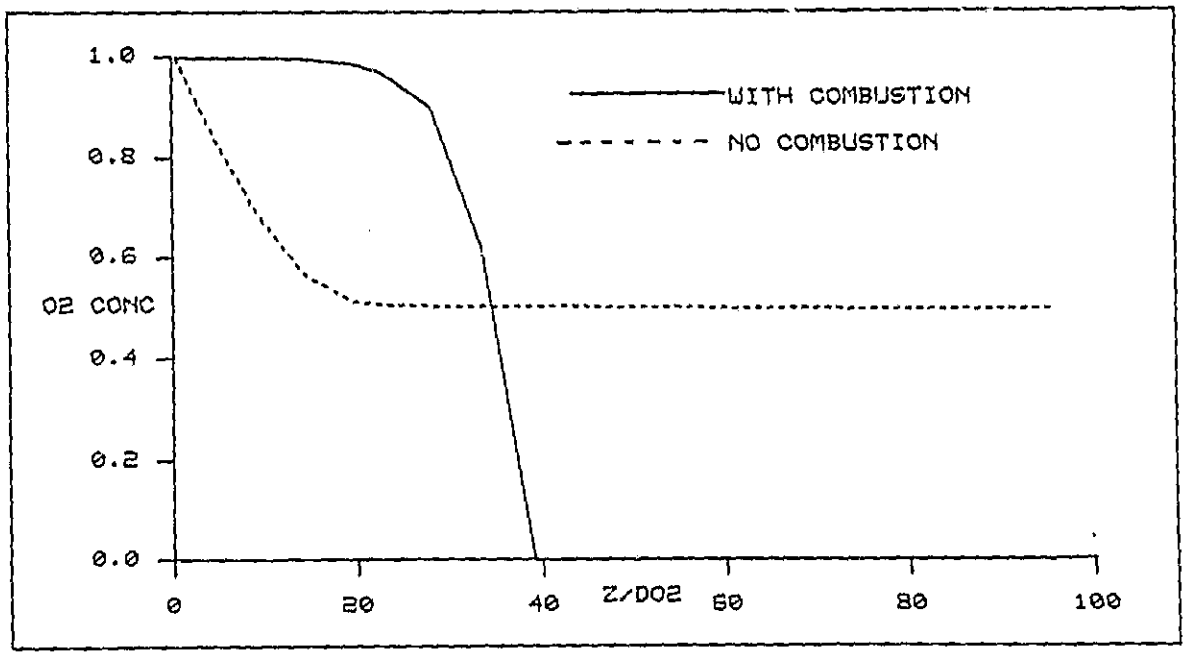

Fig.5: Variation of O_2 concentration at the centerline (r = 0)

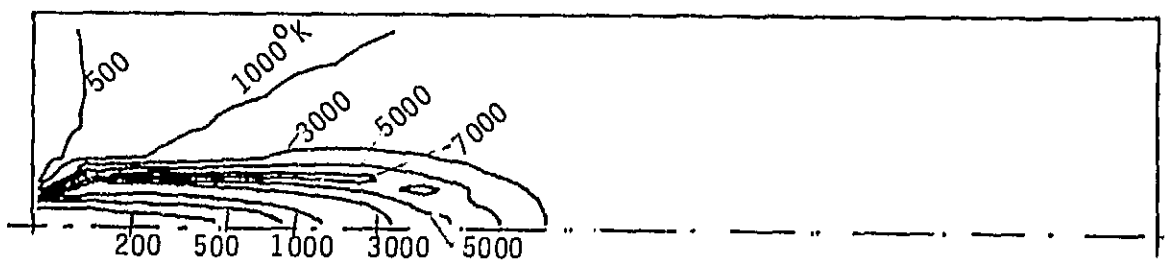

Fig.6: Temperature Contours for the combusting case

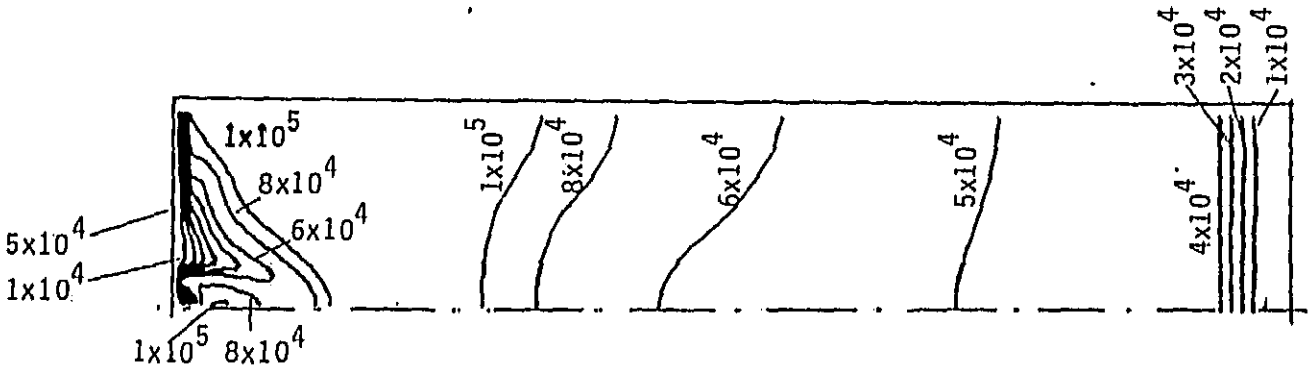

(a) No Combustion

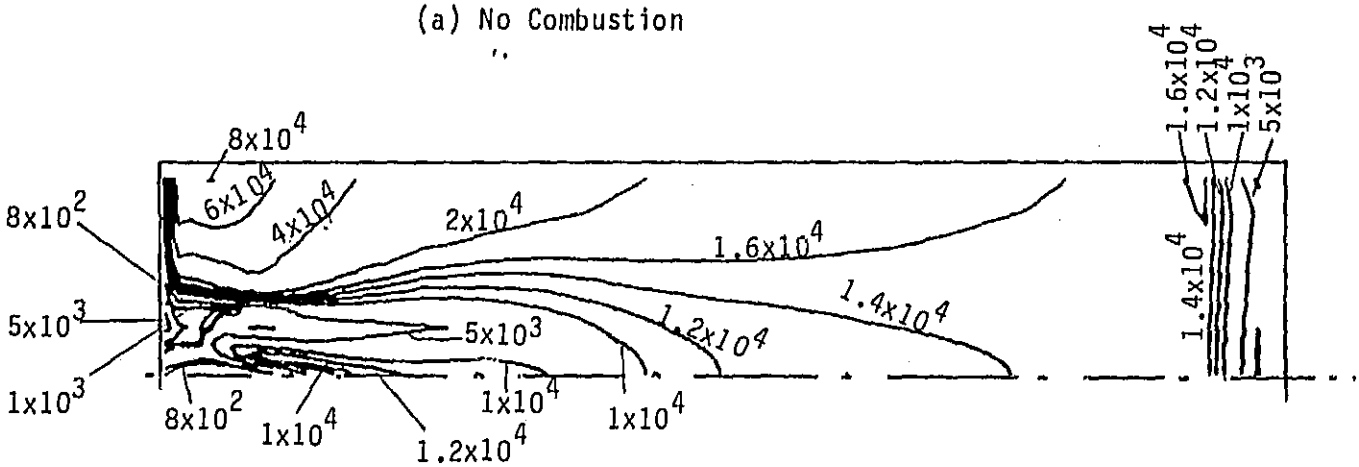

(b) With Combustion

Fig.7: Contour levels of $\mu_{eff}/\mu_{\ell am}$

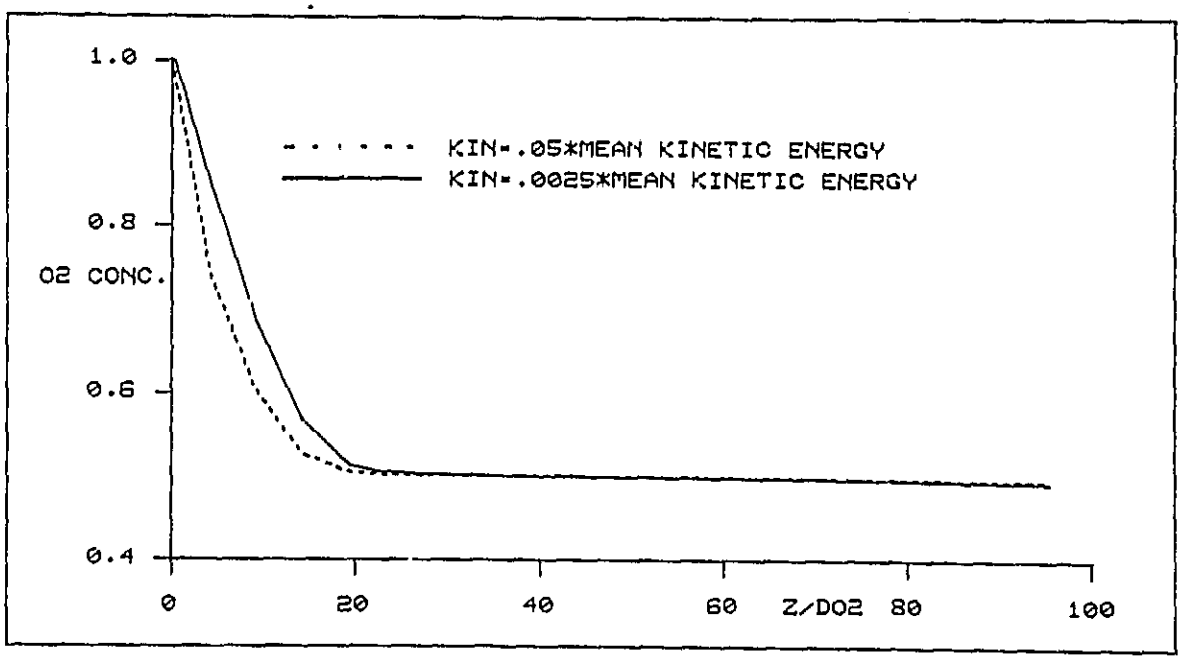

Fig.8: Variation of O_2 concentration at the centerline. Effect of the turbulent kinetic energy at inlet. Non-reacting (no combustion) case.

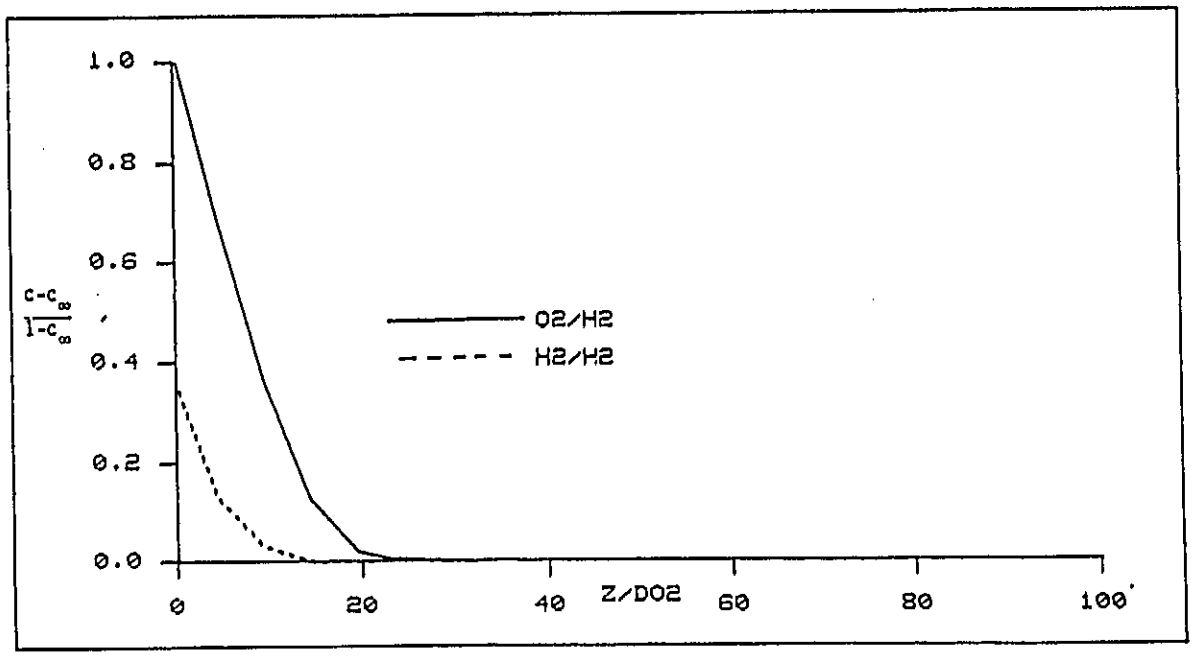

Fig.9: Concentration at the centerline. Effect of the density difference between the jets. Non-reacting flow.

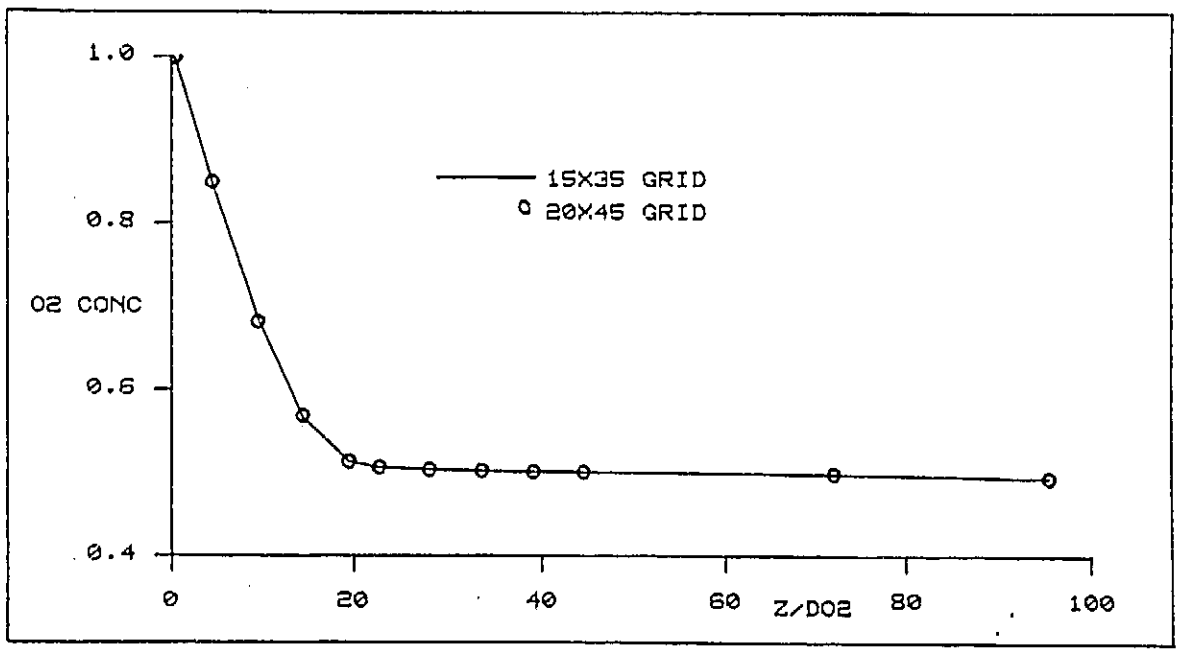

Fig.10: Grid refinement study. O_2 concentration at the centerline. Non-reacting (no combustion) case.

CHAM

CHAM OF NORTH AMERICA

APPENDIX 3

INTERIM REPORT

on

Global Modeling of SSME

by

T. Mukerjee and A. Przekwas

ABSTRACT

For global modeling, the SSME has been divided into various sections and the present report is on the first cut 3-D analysis of the Main Injector Assembly section containing the LOX posts wherein gases enter from the fuel-side transfer ducts and also from the oxidiser-side transfer ducts. The gases escape through the holes on the injector body into the main chamber. Two calculations, one with and the other without LOX post shields, have been performed. The results seem plausible and show strong influence of the shields. Further analysis and security of results are in progress.

1. INTRODUCTION

For global modeling of the SSME, the unit may be divided into various major sections as shown in Figure 1. A one-dimensional model is in use at NASA for predicting the global flow parameters for steady and transient cases. Since the flows in many components of SSME are far from one-dimensional, 2D or 3-D analyses are needed for better understanding of their performances. The present work is under taken with that very objective in view.

The section of the SSME where immediate attention is focussed is the region bounded by dotted line in Figure 1. In Figure 2 the components of interest are shown with indications of the type of analysis (1-D or 3-D) and the types of input/output data processors required in between some of the components. The present task is concerned with the 3-D analysis of the Main Chamber Injector Assembly (MIA) with the LOX posts. The results are shown as vector and contour plots of various flow parameters for two cases; first, without shields on the LOX posts at the periphery, and, second, with shields. They show significant effects of the shields and seem plausible.

2. THE GEOMETRY CONSIDERED

Figure 3 shows the cross-sectional views of the LOX post region in the Main Injector Assembly (MIA). Within the MIA there are 600 injector elements distributed as shown in Figures 3 and 4. Of these, 75 are baffle elements while the others are main elements (Figure 4) and their constructions are shown in Figures 5 and 6 respectively. The baffle elements let the coolant H_2 from the region between primary and secondary plates out into the main combustion chamber (see Figure 5). They are longer than the main elements. Both these types of injectors have a central tube for oxidizer flow and a concentric annular passage for the fuel to flow into the main combustion chamber. The entry holes for fuel in each type of element are different as shown in Figures 5 and 6.

3. COMPUTATIONAL DETAILS

Figures 7(a) and (b) show the calculation domain with the transfer ducts from fuel and oxider sides discharging into it and the grid used. Due to symmetry a 180^0 sector of the MIA has been simulated with NX = 10, MY = 14 and NZ = 11 computational grid.

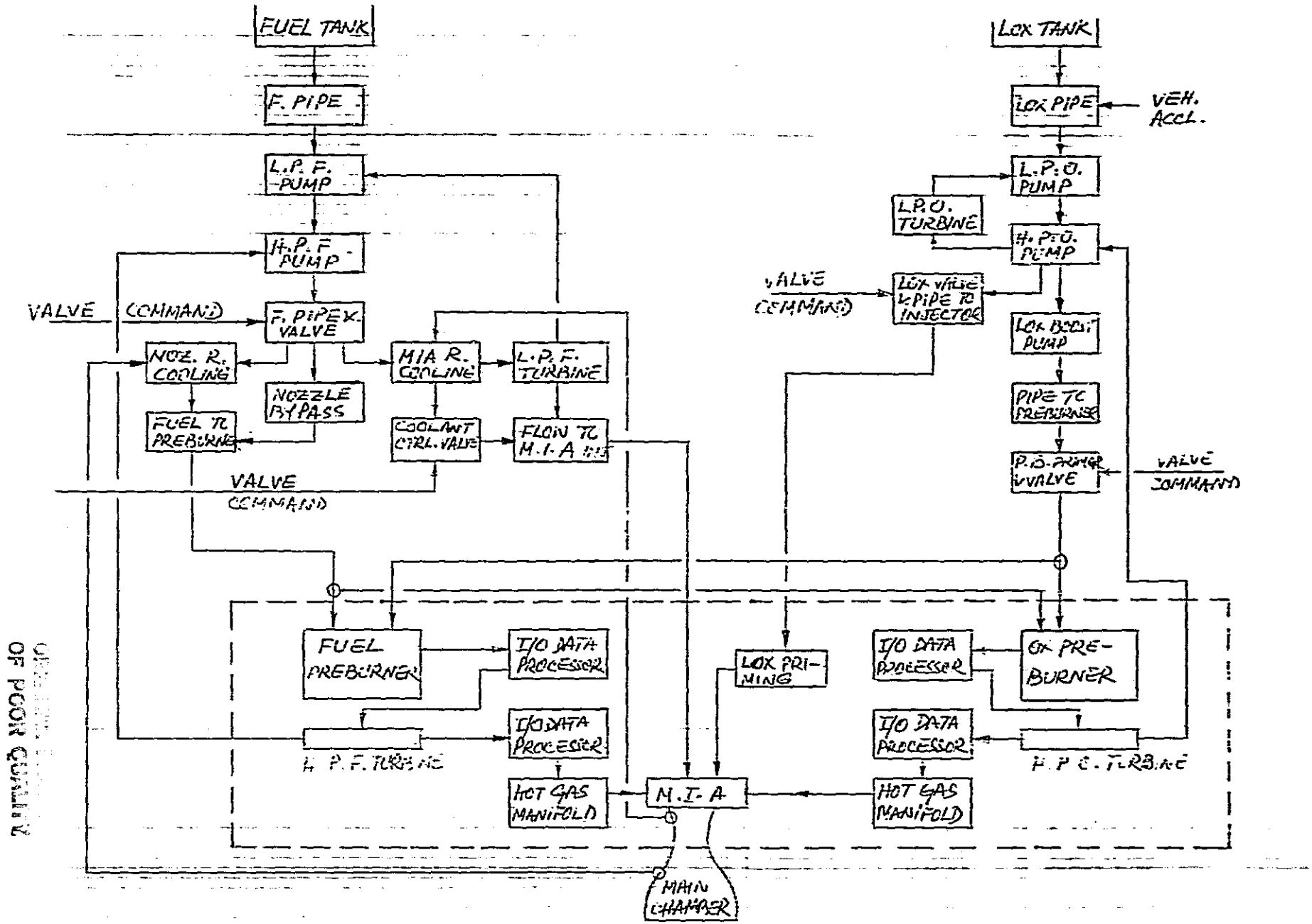

Figure 1. Flow Diagram for SSME Global Model Analysis

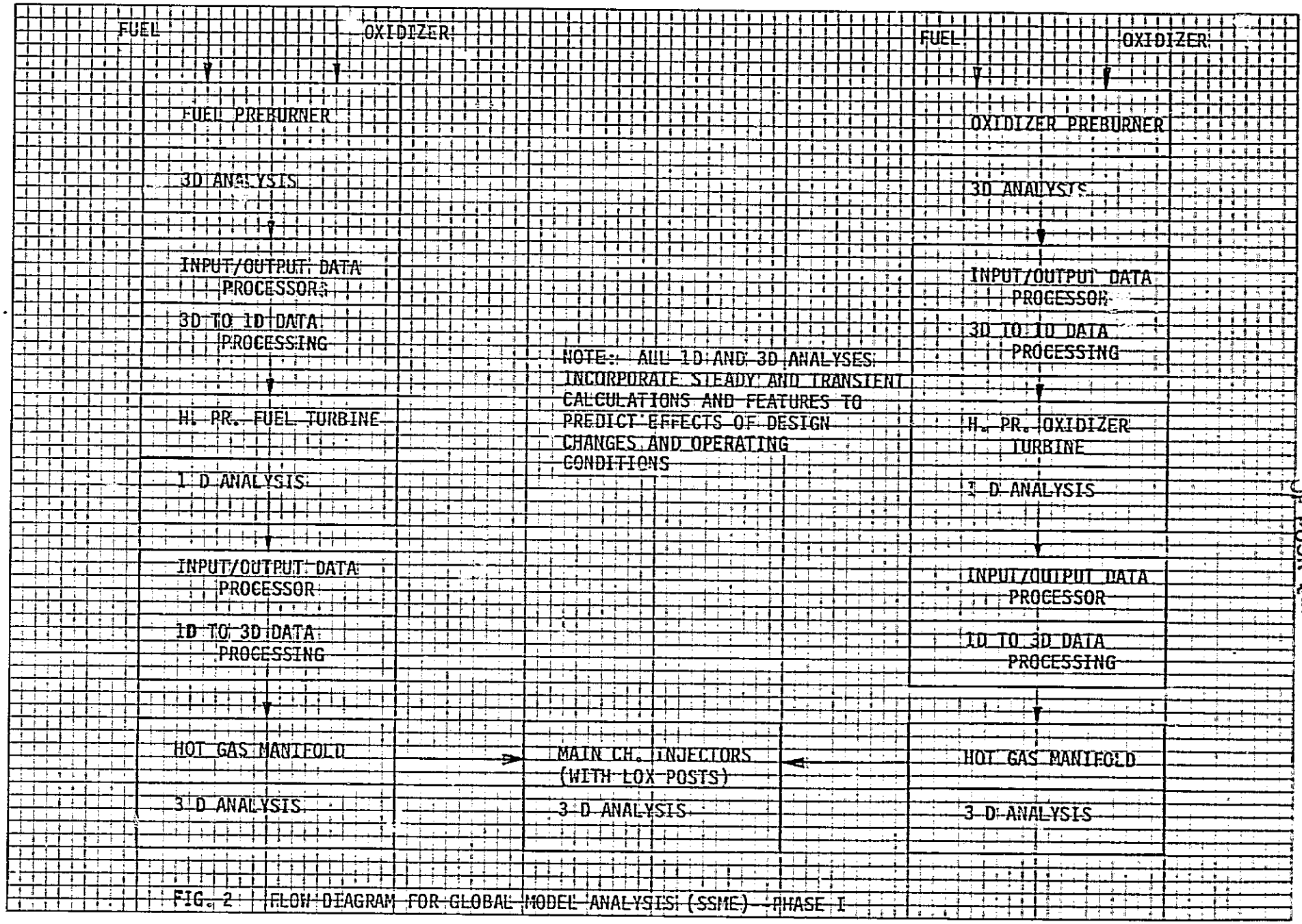

FIG. 2 FLOW DIAGRAM FOR GLOBAL MODEL ANALYSIS (SSME) - PHASE I

POWERHEAD ASSEMBLY

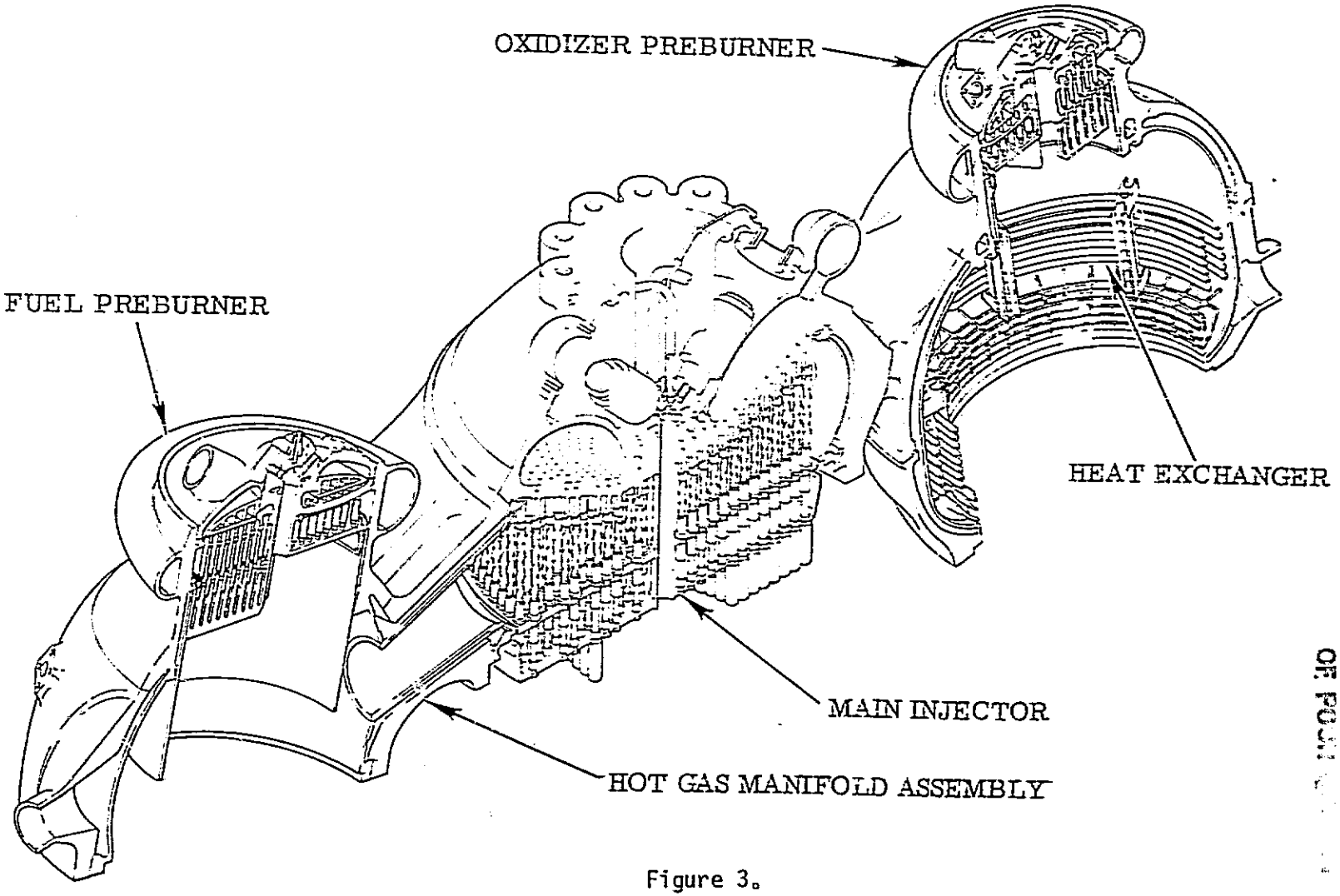

Figure 3.

MAIN INJECTOR ASSEMBLY

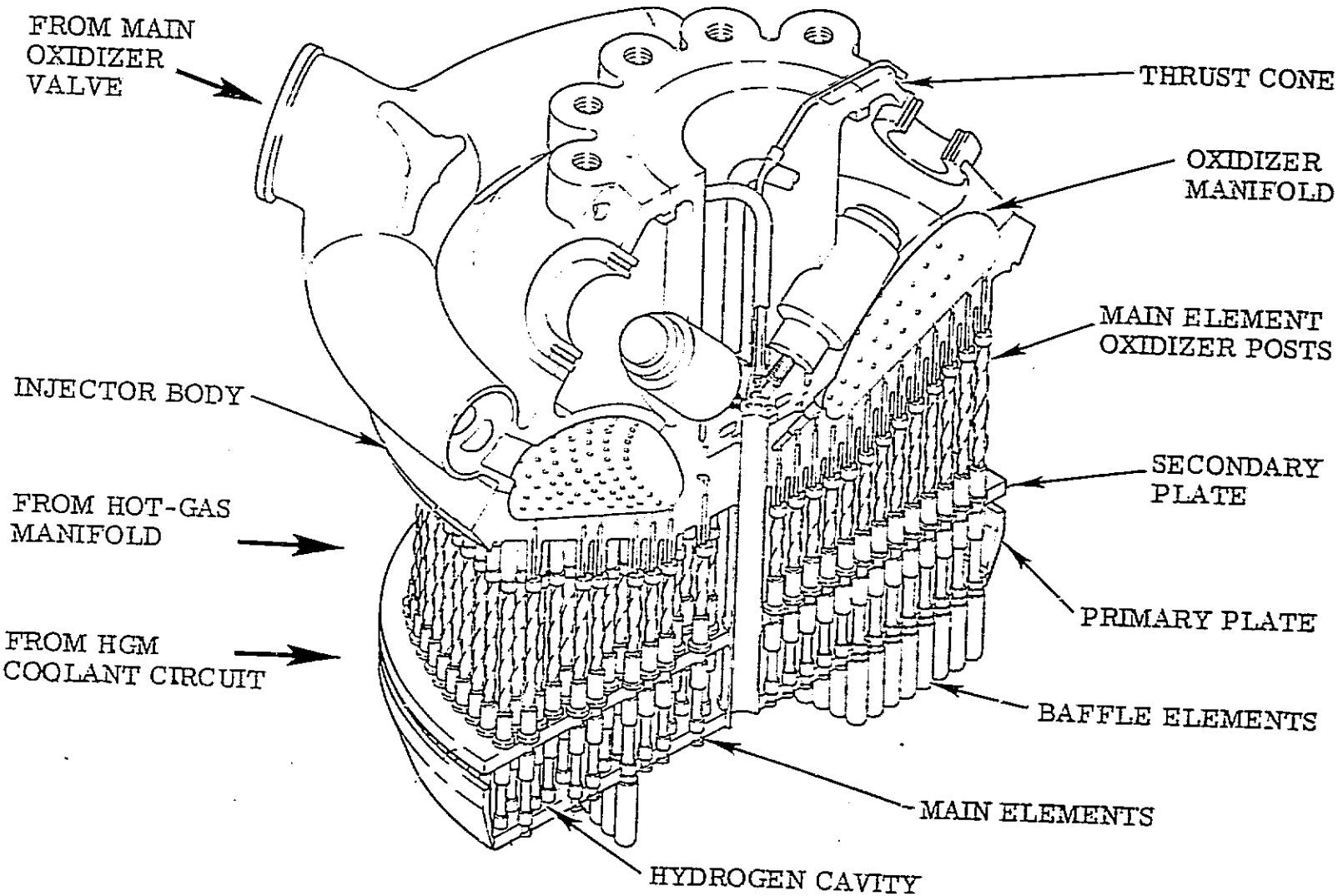

Figure 4.

MAIN INJECTOR BAFFLE ELEMENT

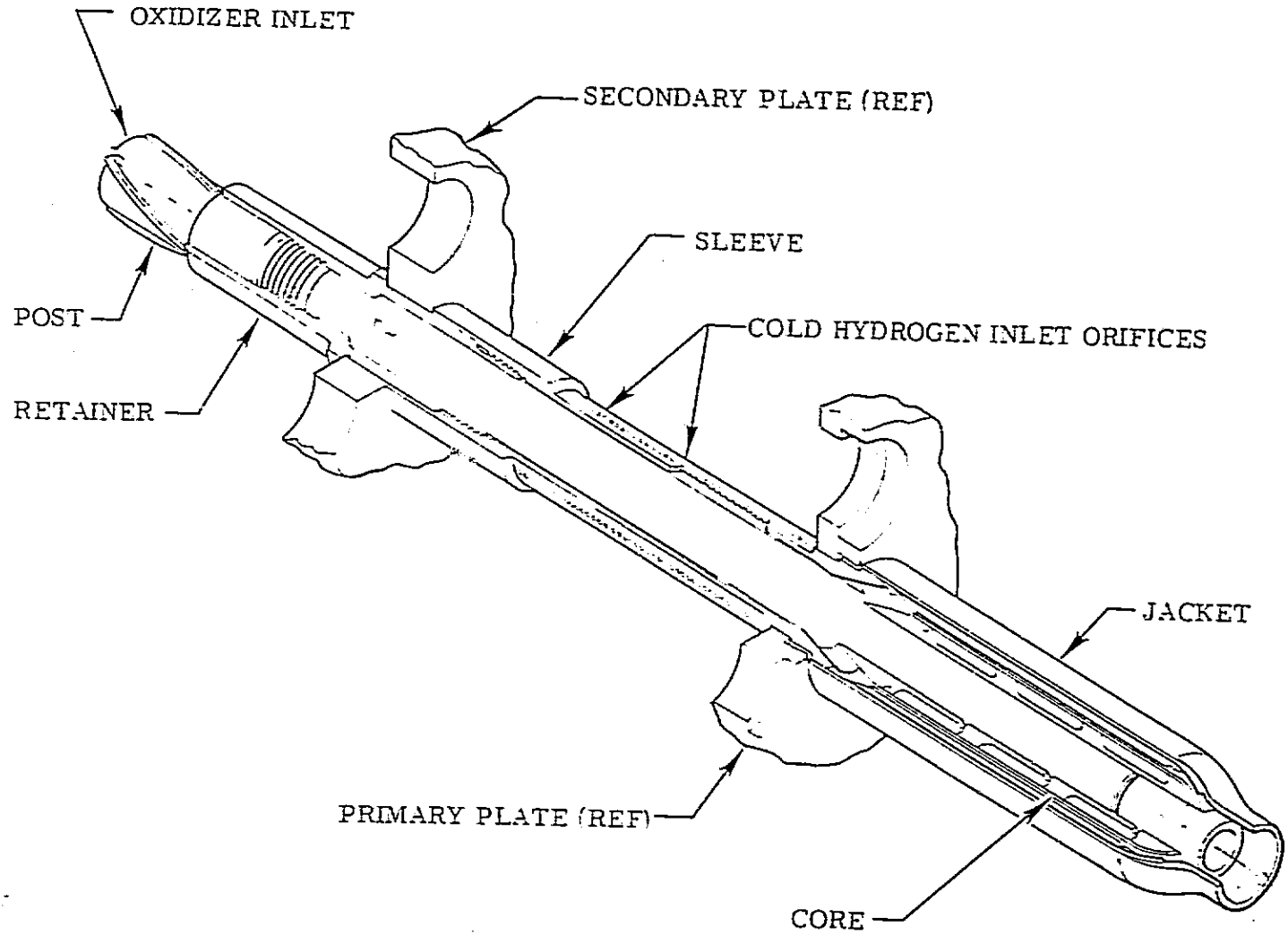

Figure 5.

MAIN INJECTOR ELEMENT

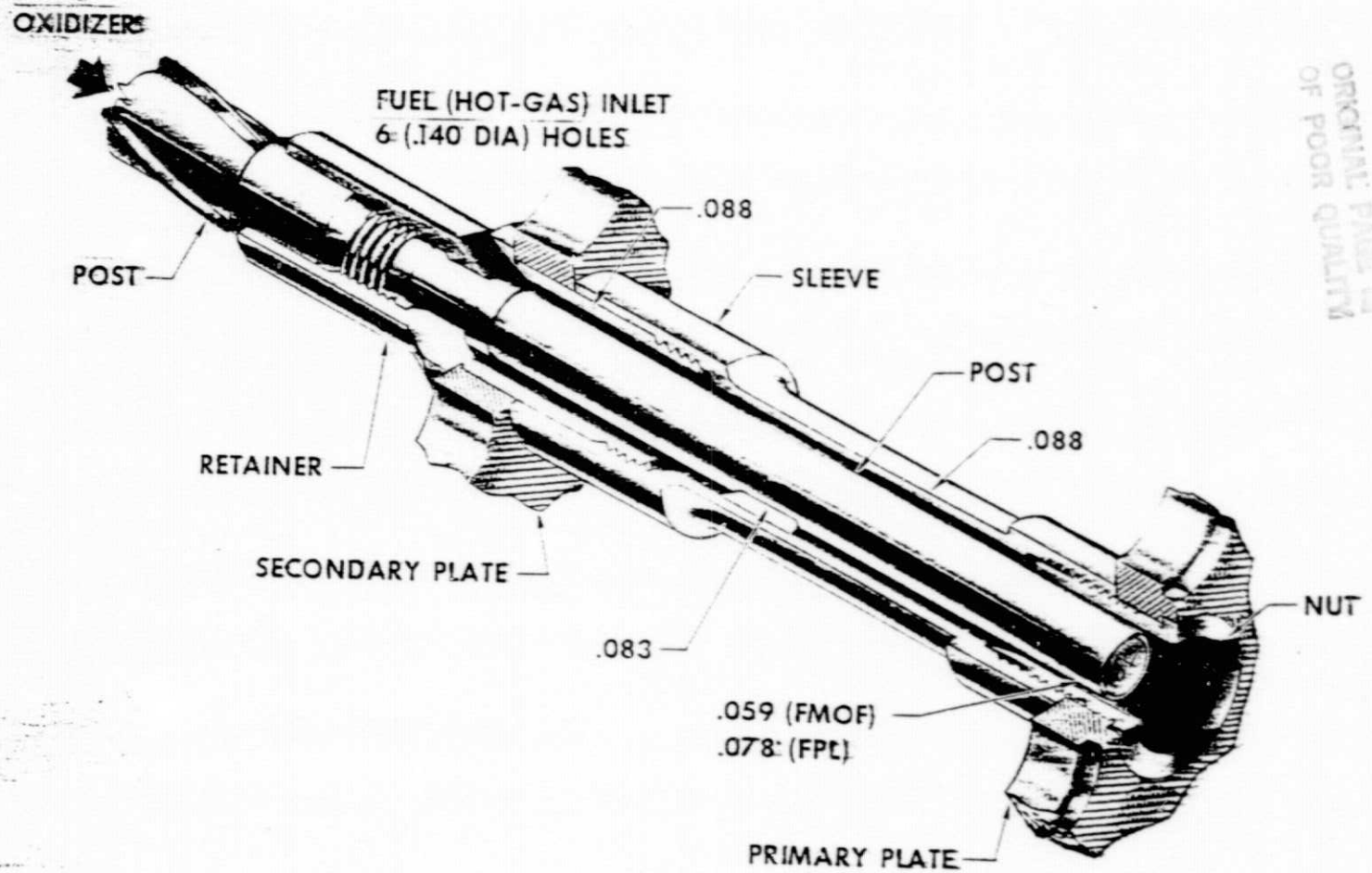

Figure 6.

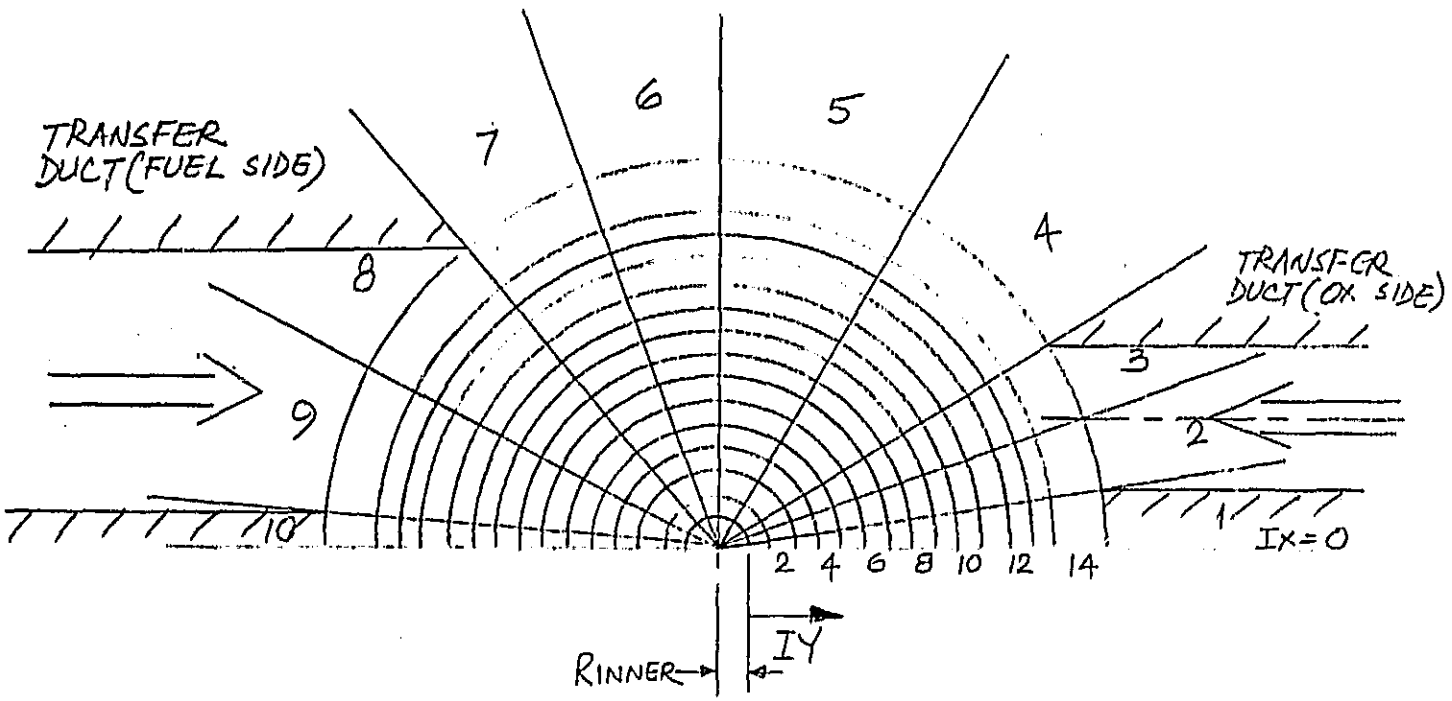

a) GRID - PLAN VIEW (XY PLANE)

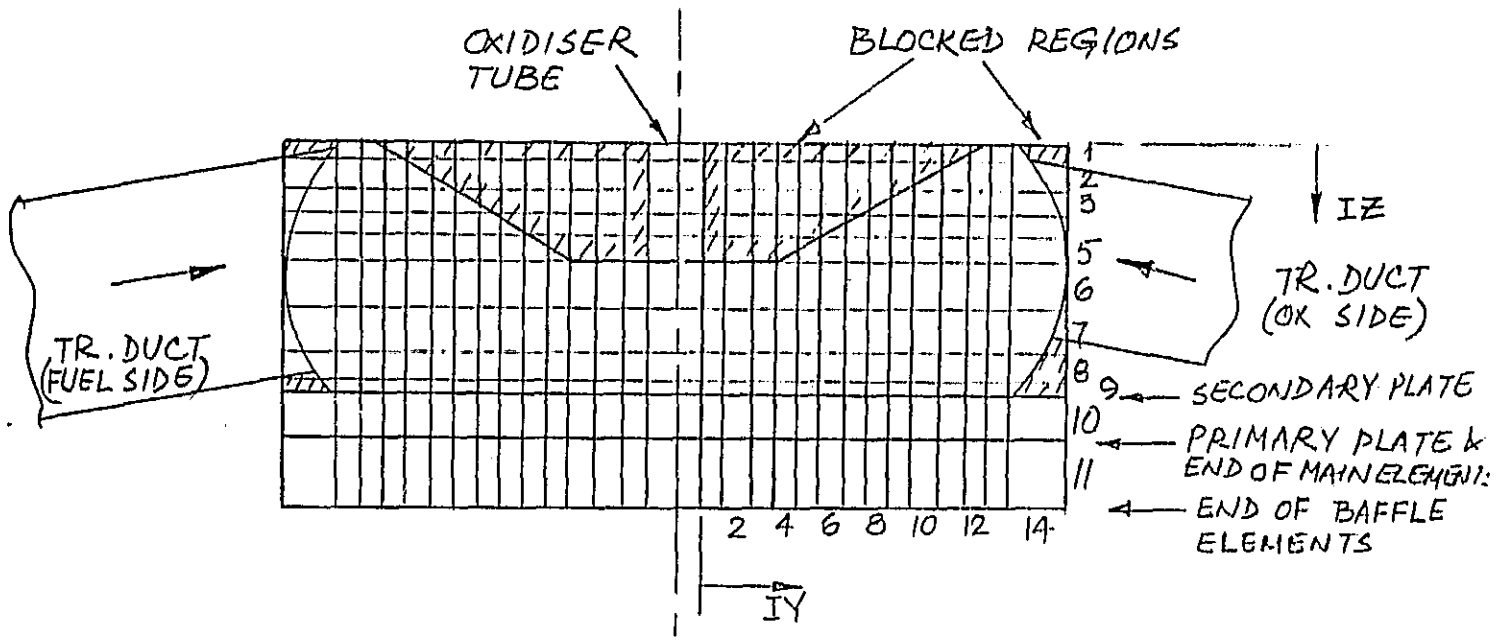

b) GRID - FRONT VIEW (YZ PLANE)

Figure 7. Grid Layout For Main Injector Assembly.

The flow is considered turbulent and incompressible and the effective viscosity is assumed to be 10^4 times the Laminar viscosity μ_L which is taken as 2.46 E-5 Ms/m^2. The density of the fluid, ρ = 22.33 kg/m^3. The calculated mass inflow from one fuel transfer duct is 40.0 kg/s and the mass inflow from oxidiser transfer duct is 15.2 kg/s. The velocities of these two streams at MIA entry are assumed uniform.

The LOX posts have been represented by appropriate volume and flow area porosities; and, likewise, the outflow openings in the main elements have been described by a specified area porosity. The "ceiling" of the MIA has been prescribed by a profile of porosities varying from 0 to 1. Since there is no outflow through the baffle elements from above the secondary plate, the high-face area porosity of the cells containing those elements is zero. Lastly, the shield plates on the outer row of LOX posts have also been described by appropriate north-face area porosity in the calculations.

The calculated values of the porosities used for various sections are as follows:

1. LOX-post section:
   East face porosity = 0.416
   North face porosity = 0.3
   High face porosity = 0.42
   Cell volume porosity = 0.42

2. Inter-plate (between secondary and primary plates) section:
   East face porosity = 0.0
   North face porosity = 0.0
   High face porosity = 0.14
   Cell volume porosity = 0.14

3. Outer LOX posts (shield mounted):
   East face porosity = 0.416
   North face porosity = 0.071
   High face porosity = 0.42
   Cell volume porosity = 0.42

The walls have been assumed adiabatic and frictionless and momentum loss due to LOX-post cluster has not been accounted for. However, the losses due

to the outflow through the annular flow passages in main elements have been taken into account using the following expression:

$$C_\ell = 0.5 \times \{(\frac{A_a}{A_i} - 1)^2 + 4 \frac{f \cdot \ell_a}{d_a}\}$$

where

C_ℓ = Loss ceofficient
A_a = Area of the annulus
A_i = Area upstream of entry to annulus
f = Friction factor (=0.003)
ℓ_a = Length of annular passage
d_a = Equivalent diameter of annulus

For the given configuration $C_\ell = 18.92$

Computations were done for two cases as follows:

a) Without shields on the outer LOX posts;

b) With shields on the outer LOX posts.

For both the cases, the exit pressure in the main chamber has been assumed constant.

4. PRESENTAITON AND DISCUSSION OF RESULTS

The results are presented and discussed for the two cases separately in two subsections, the first one dealing with flow without shields and the second one with shields on the outer row of LOX posts.

4.1 Flow Without Shields

Figures 8(a), (b) and (c) show velocity vector plots in MIA at selected planes. Figure 9 shows the concentration contours which indicate the extent of mixing between the two streams entering MIA from fuel and oxidiser sides respectively.

The vector plots in Figures 8(a) and (b) clearly exhibit dominant role of the stream from the fuel (F) side as it changes into the oxidiser (OX) side. The flow in the race track region is circumferential nearer to the roof of MIA and tends

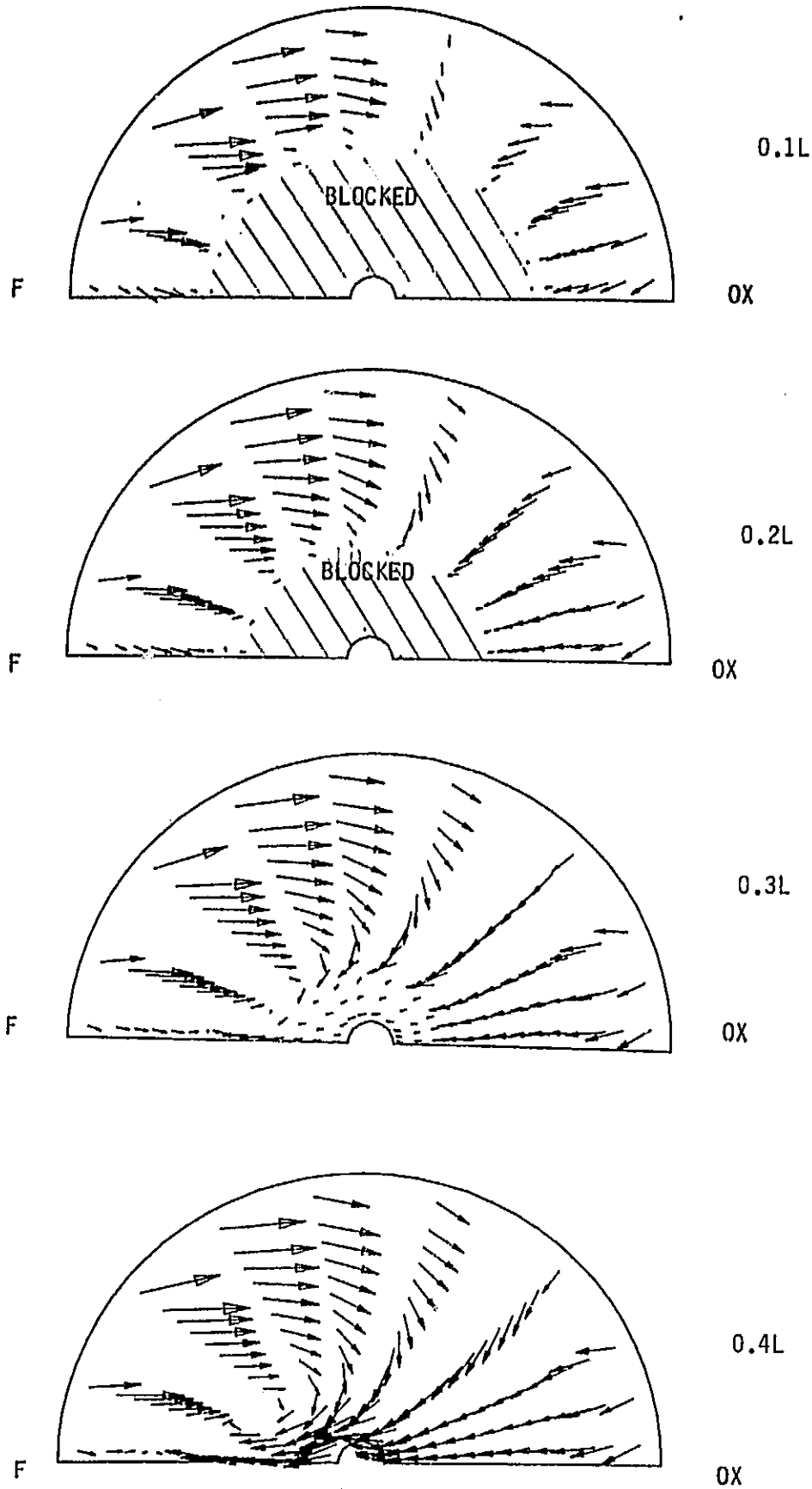

Figure 8(a). Velocity Vector Plot in MIA - No Shields

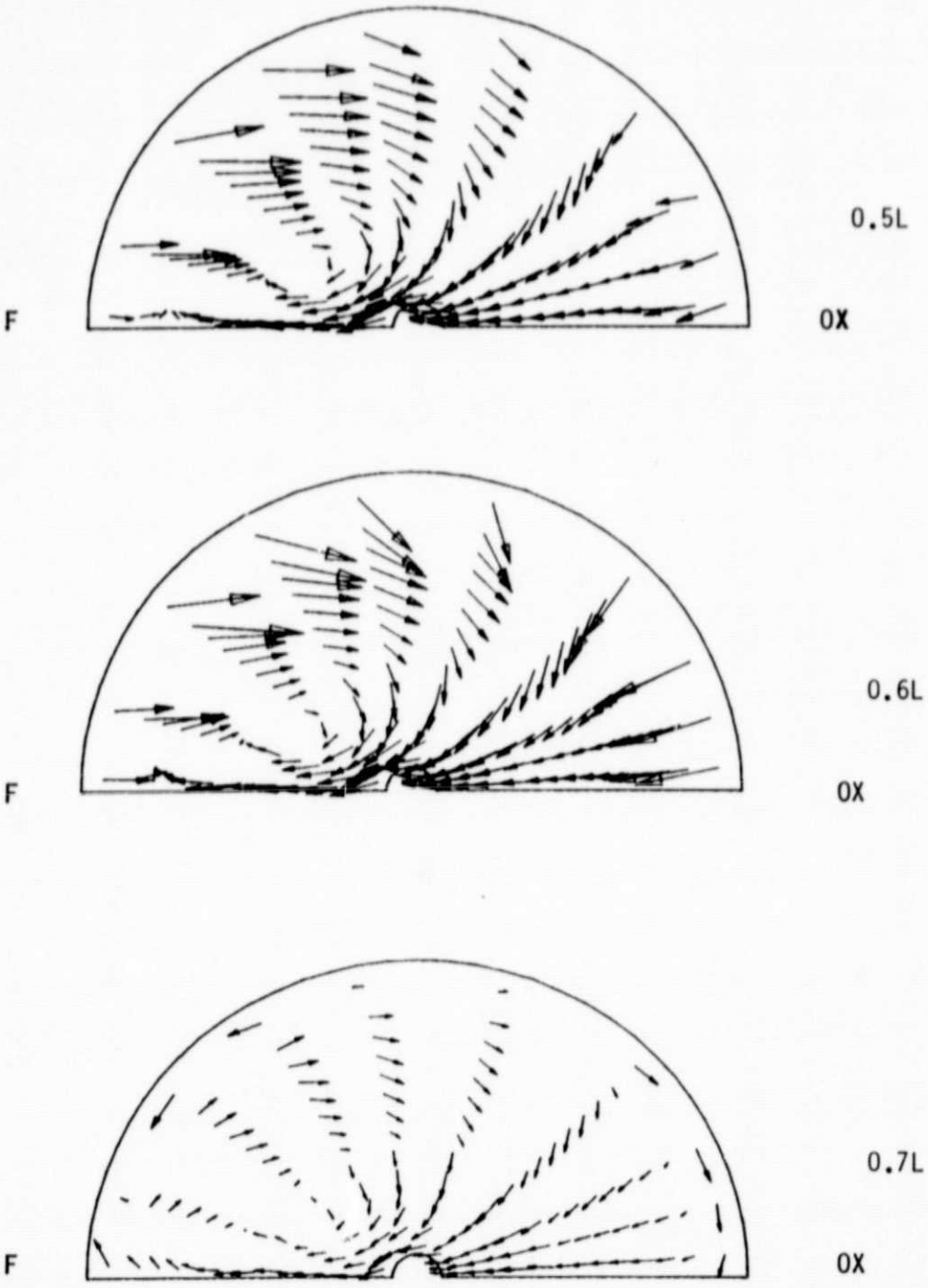

F = Fuel Side
OX = Oxidiser Side

L = 10 in
= Length of Calculation in Z direction

Figure 8(b). Velocity Vector Plot in MIA - No Shields

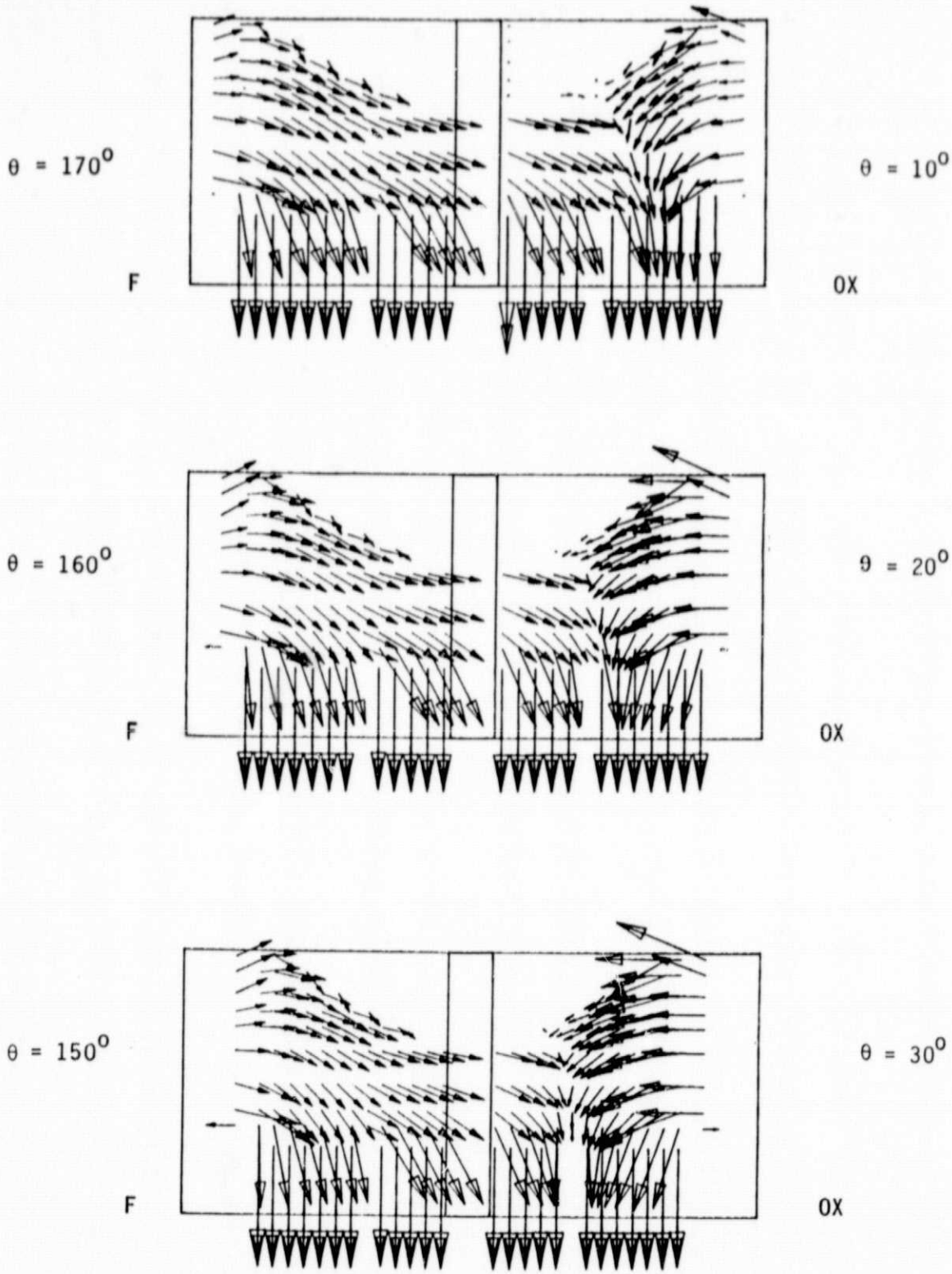

Figure 8(c). Velocity Vector Plot in MIA - No Shields

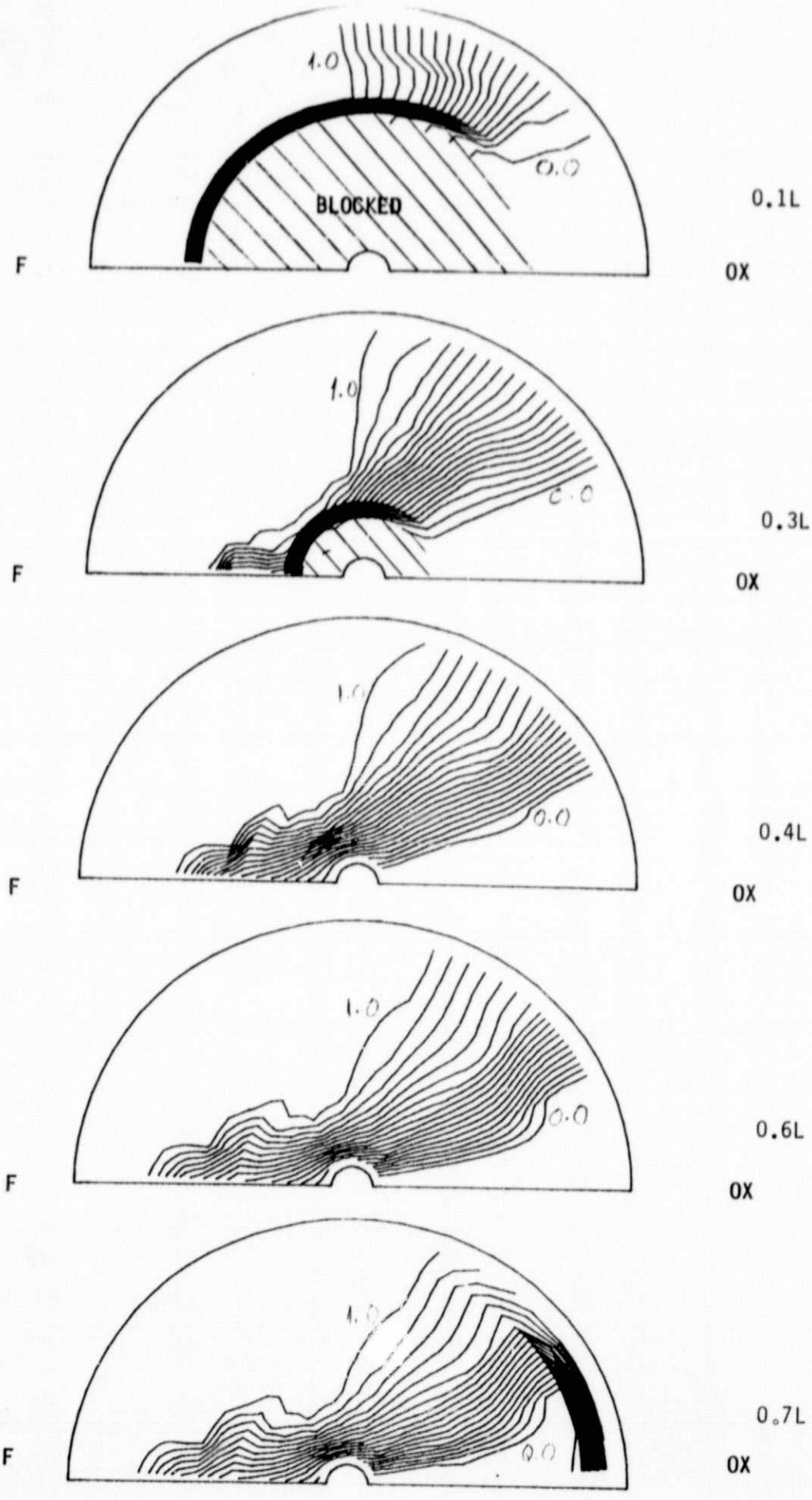

Figure 9. Concentration Contour Plots in MIA - No Shields

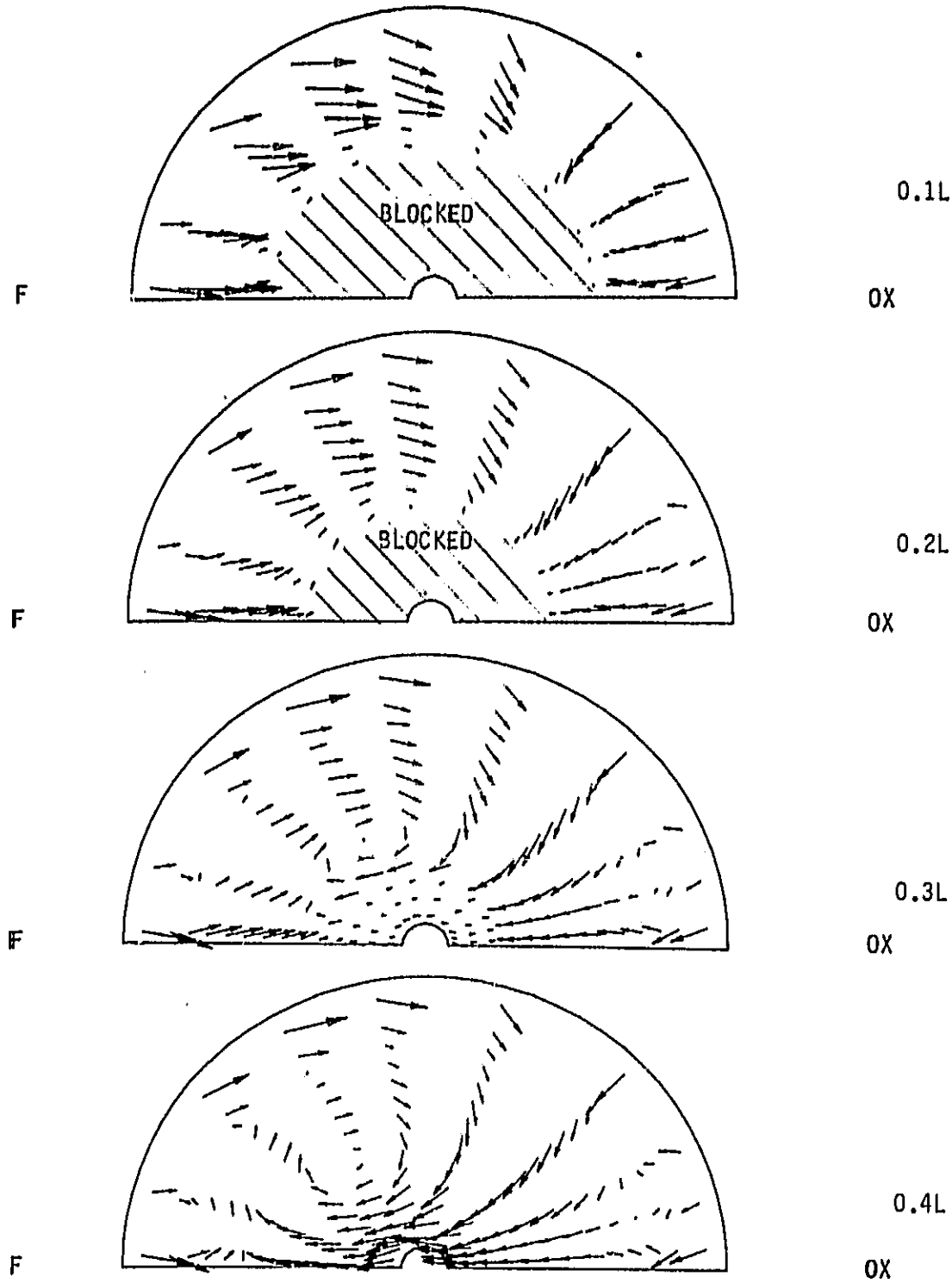

Figure 10(a). Velocity Vector Plot In MIA - With Shields

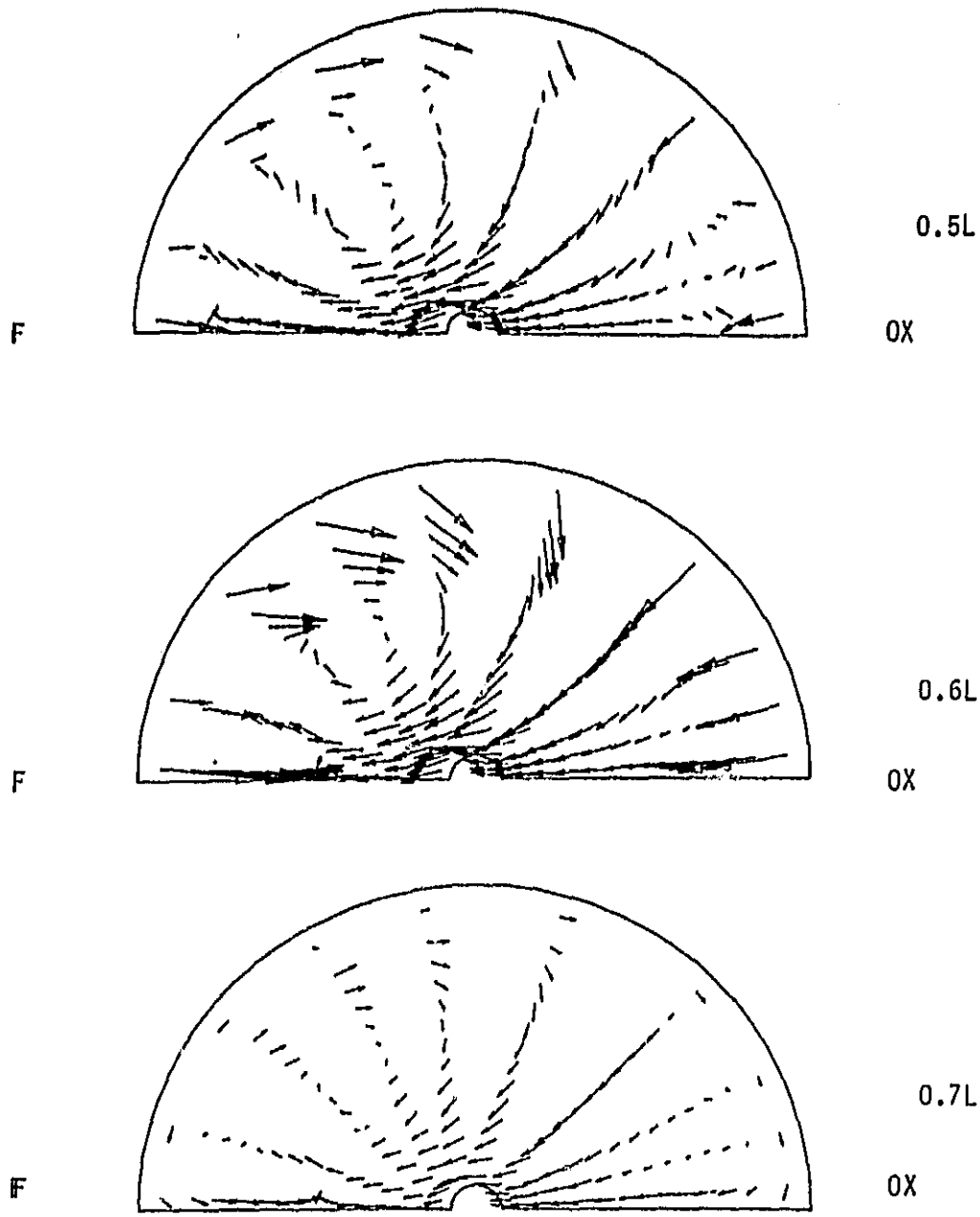

F = Fuel Side
OX = Oxidiser Side

L = Length of
Calculation domain
in Z direction
= 10 in.

Figure 10(b). Velocity Vector Plot in MIA -
With Shields.

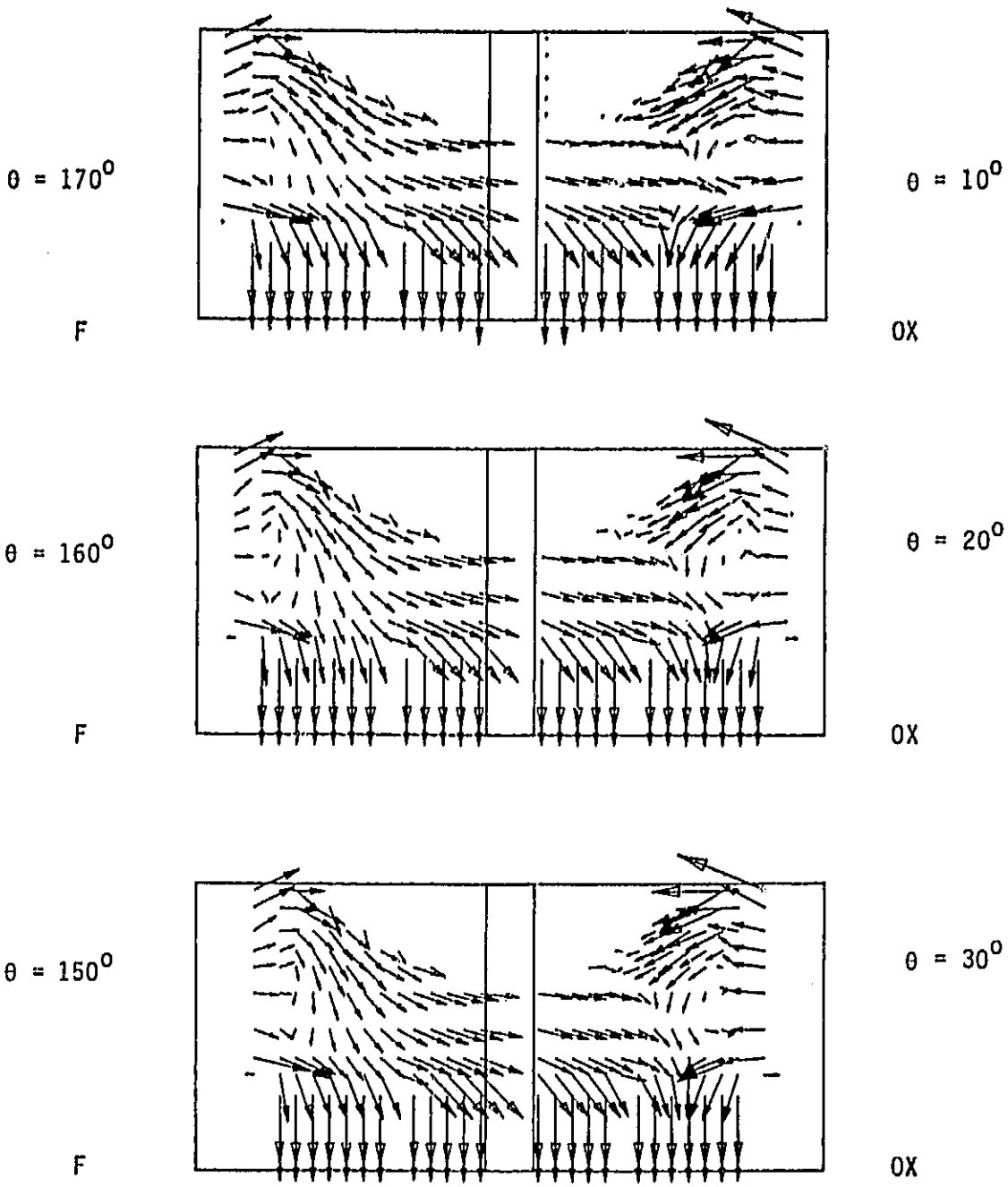

Figure 10(c). Velocity Vector Plot in MIA - With Shield.

to be more radial at 0.6L. At 0.7L the circumferential flow direction shows a remarkable change primarily because of the significant blockage of the secondary plate. The stream from the Oxygen side, however, penetrates deep into the MIA axis region; and, mixing with the stream from F side it axially penetrates into the F side. A small stagnation region is produced as this stream gets close to the wall and the fluid recirculates there. This could be responsible for a greater tendency of a circumferential flow on F side than on OX side.

Figure 8(c) shows, as above, the dominant nature of the flow from F side which is mainly due to a larger mass airflow from there. The vectors on the OX side entry appear longer than on F side in the plot mainly because of a radial direction of the flow on OX side compared to a mostly circumferential type on F side. The restricted outflow area in the main elements increasing the local velocities at the lower end of the calculation domain.

Figure 9 presents the mixing pattern within the MIA in terms of mass fraction contour lines for the fluid injected from the F side. From the development of the mixing pattern it is visible that even at the secondary plate level there exists a large area of unmixed fluids. The concentration gradients are, however, smaller than those in the upper part of the MIA.

4.2 Flow With Shields

Figures 10(a), (b) and (c) show velocity vector plots in MIA at selected planes. Figure 11 shows the concentration contours which indicate the extent of mixing between the streams entering the MIA.

The vector plots in Figures 10(a) and (b) clearly show the effect of the shields in restricting the flow in the radial direction at the two entries and turning it more in the circumferential direction. As a result a larger recirculation region is produced on the F side compared with the case of no-shields in Figures 8(a) and (b). Since the shields leave portions at the top and bottom of the LOX posts uncovered, the flow velocities at 0.1L and 0.6L at entry region are higher than elsewhere as is evident in Figure 10(c).

Behind the shields there are recirculation regions (Figure 10(c)), particularly near the OX side entry, and, this also shows almost 10 times the pressure drop observed with no-shield case. Such features will obviously produce significant

bending stresses on the LOX posts which support the shields there.

Figure 11 shows the concentration contours in MIA. They are similar to those shown in Figure 9 although there are some differences on the F side due to a larger recirculation in the flow field with shields.

4.3 Comparison of the Flow Fields With and Without Shields.

Figure 12 demonstrates the differences in the MIA flow field as a result of the use of LOX post shields. As already mentioned, there are recirculating flows behind the shields particularly at the entry regions and also less uniform distribution of flow across the whole vertical planes there. On account of large circumferential flow in the race track, there is a greater penetration of the fluid rom F side to OX side and this is evident in the contours of concentration shown for the case with shields.

5.0 CONCLUSIONS AND RECOMMENDATIONS

- The computed flow fields seem plausible in line with the assumptions.
- The main effect of the LOX-post shields is extra loading of the LOX posts due to flow non-uniformities and large pressure difference across them. These also create recirculation regions which are expected to increase local turbulence levels and pressure fluctuations, and may not be desirable features.
- The recommended model refinements, in the order of priority, are:

  a) Use of a more realistic value of eddy viscosity (μ_{eff}). For example, $\mu_{eff} = C \cdot \frac{\rho v \ell}{\mu}$, where C is an empirical constant (of the order of 0.01) and ℓ is the characteristic geometry length (for example, gap between two posts).

  b) Inclusion of axial and cross flow resistances due to LOX posts in the region above the secondary plate.

  c) Non-uniform inlet velocities, estimated from the results of hot gas manifold analysis.

  d) Refinements in the representation of the entry faces from transfer ducts.

  e) Finer grid distributions to determine the sensitivity of results.

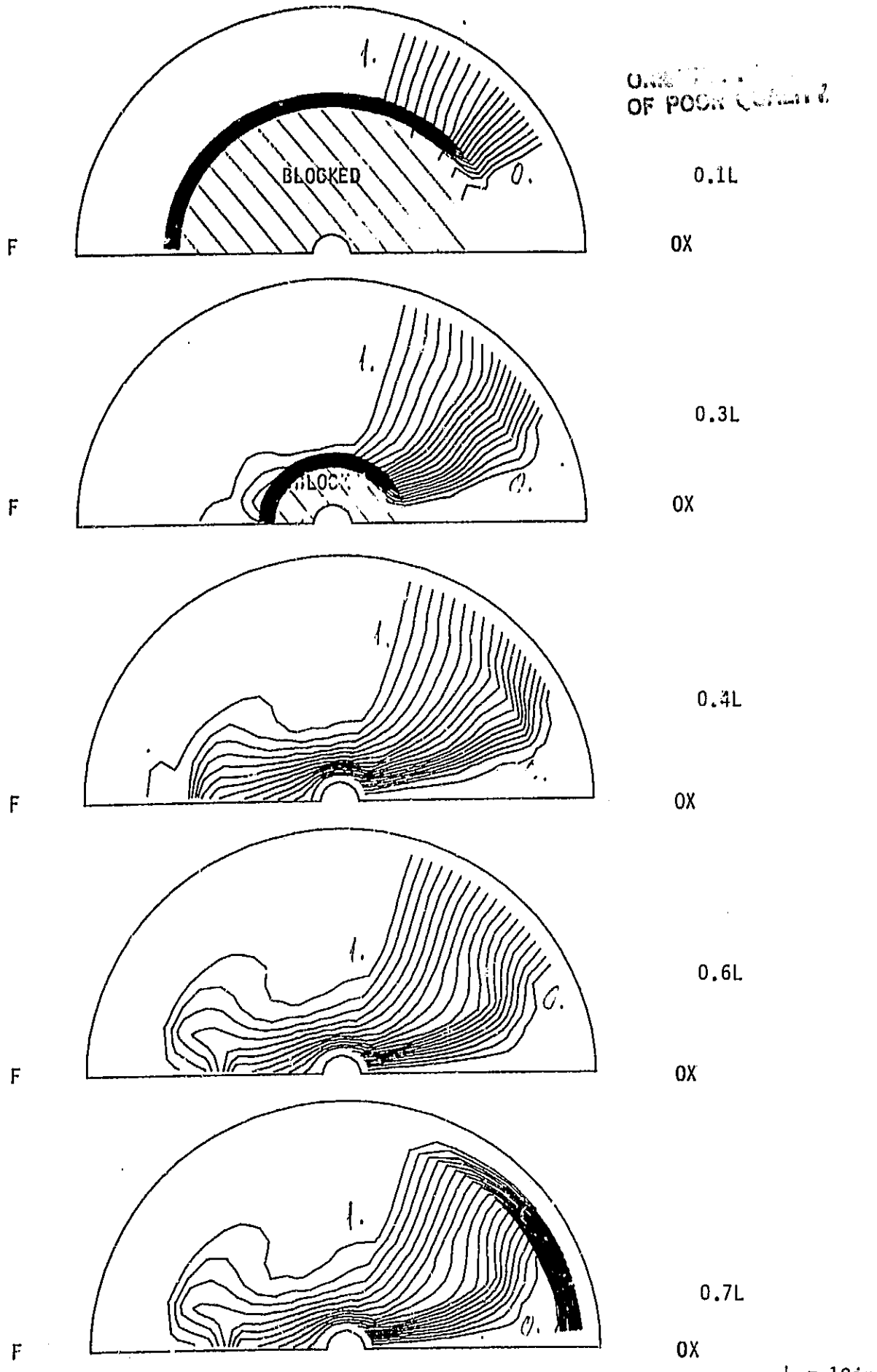

Figure 11. Concentration Contour Plots in MIA - With Shields

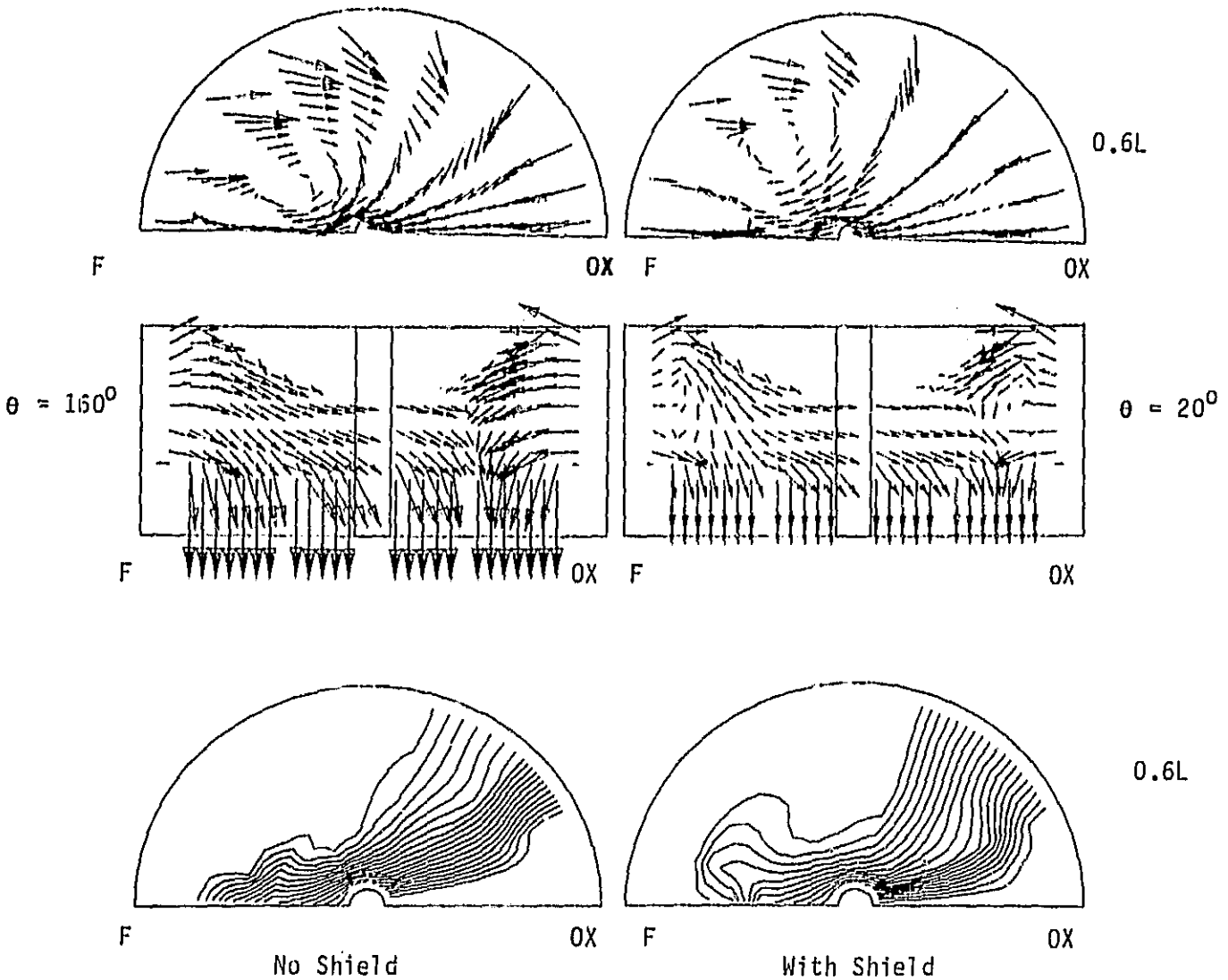

Figure 12. Comparative Study of Flow Fields In MIA Without and With Shields on LOX posts.